Opto-acoustic Coupling in a Pristine Crystal via Brillouin Scattering

PhD thesis by

Sissel Bay Nielsen

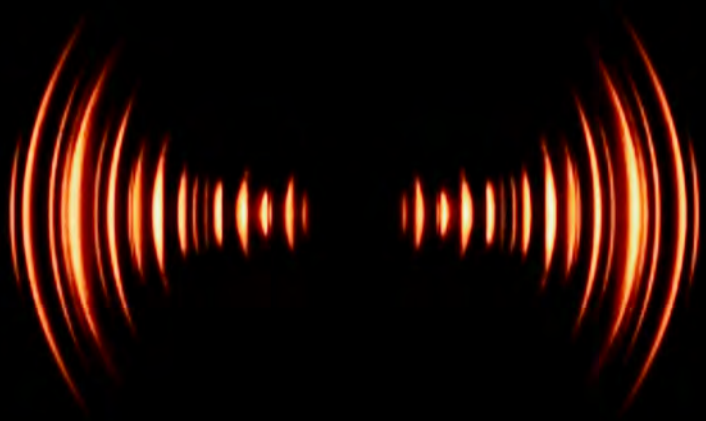

December 2022

Technical University of Denmark
Department of Physics
Fysikvej, Building 307
2800 Kongens Lyngby, Denmark
www.fysik.dtu.dk

Opto-acoustic Coupling in a Pristine Crystal via Brillouin Scattering

A Thesis Submitted in Partial Fulfilment of the Requirements for the Degree of Doctor of Philosophy in Physics

Sissel Bay Nielsen

December 2022

Department of Physics
Technical University of Denmark

Principal Supervisor:	Professor Ulrik Lund Andersen
Co-supervisor:	Senior Advisor Ulrich Busk Hoff
Co-supervisor:	Associate Professor Jonas Schou Neergaard-Nielsen

Abstract

In this thesis, coupling between optics and acoustics in an optomechanical cavity is reported. The coupling is established via Brillouin scattering of light at telecom wavelengths (1550 nm) scattered from high frequency bulk acoustic waves ($\sim$ 12 GHz) in crystalline quartz. Two optomechanical cavities are presented; one for operation at room temperature, the other for operation at milli-Kelvin temperatures. Further, simulations of the advantageous asymmetric mode spacing of the cavities and the physical criteria for the constructions are carried out. At room temperature, Brillouin lasing is obtained with a lasing threshold of 15 mW. Furthermore, strong coupling between the hybridised optical and acoustic modes is demonstrated at different input powers, allowing for the estimation of a single photon coupling rate of $g_0/2\pi \simeq (1.2 \pm 0.2)$ Hz. The strong coupling demonstrated at room temperature in this work is an important milestone building towards achieving strong coupling at milli-Kelvin temperatures. The latter is of huge interest as it will allow for quantum coherent state transfer which in turn will open the door to interrogating alternative theories of physics e.g., quantum phenomena in macroscopic objects, and hybrid quantum technologies, such as quantum memories and quantum transducers. Therefore working towards this direction, finally, the design of a state-of-the-art cavity for ground state operation as well as its characterisation is presented.

Dansk Resumé

I denne afhandling, er interaktionen mellem optik og akustik i en optomekanisk kavitet præsenteret. Interaktionen etableres via Brillouin spredning af lys i telekom bølgelængder (1550 nm) spredt fra høj-frekvente bulk akustiske bølger ($\sim$ 12 GHz) i krystallinsk kvarts. Der er præsenteret to optomekaniske kaviteter; en til eksperimenter ved stuetemperatur, den anden til eksperimenter ved milli-Kelvin temperaturer. Simuleringer af de fysiske kriterier for kaviteterne er desuden præsenteret samt den fordelagtige asymmetri af de optiske modes i kaviteten. For eksperimentet i stuetemperatur, er Brillouin laserstråling blevet påvist med en laserstrålings-tærskel på 15 mW. Derudover er der demonstreret stærk kobling mellem de hybride optiske og akustiske modes. Koblingen blev demonstreret for forskellige inputeffekter, som muliggør at estimere en enkel-foton-koblings-rate på $g_0/2\pi \simeq (1.2 \pm 0.2)$ Hz. Påvisningen af stærk kobling er en vigtig milepæl, idet det muliggør overførsel af kohærente tilstande. Når stærk kobling er opnået ved milli-Kelvin temperaturer vil det muliggøre overførsel af kohærente kvante-tilstande, hvilke vil åbne døre til at undersøge alternative fysiske teorier, bl.a. kvante-fænomener i makroskopiske objekter, samt muliggøre hybride kvante-teknologier, såsom kvante-hukommelser og kvante-transducere. Endelig er designet af en state-of-the-art kryogenisk kavitet til eksperimenter ved grundtilstanden præsenteret samt karakteriseringer af denne kavitet.

Preface

This thesis was prepared at the department of Physics at the Technical University of Denmark in partial fulfillment of the requirements for acquiring a PhD degree in physics. The work was carried out in the Quantum Physics and Information Technology (QPIT) section, Center for Macroscopic Quantum States (bigQ), with financial support from the Danish National Research Foundation.

Principal Supervisor:	Professor Ulrik Lund Andersen
Co-supervisor:	Senior Advisor Ulrich Busk Hoff
Co-supervisor:	Associate Professor Jonas Schou Neergaard-Nielsen
PhD committee:	Research Group Leader Birgit Stiller
	Associate Professor Tristan Briant
	Associate Professor Tobias Gehring

Kongens Lyngby, December 2022

Sissel Bay Nielsen

Acknowledgements

First and foremost I would like to give a sincere thank you to Ulrik Lund Andersen for his support and guidance throughout my PhD and for providing me the opportunity to pursue research in this exciting field. I definitely learned a lot under his supervision. I also want to send my gratitude to Ulrich Busk Hoff for his guidance and support as well as for his creative ideas when debugging the experiments, and for including me in his quantum outreach for kids. Thanks to Jonas Schou Neergaard-Nielsen for the always nice discussions about physics, statistics, and everything in between and for his great inputs and support.

Throughout my PhD, I have been so lucky to work in close collaboration with two dedicated and supportive postdocs. For the first third of my PhD, with Joost van der Heijden, who initiated the project and kept being supportive long after he left it. I see him as both a mentor and a friend. For the last third of my PhD, Santiago Tarrago Velez joined the project with his great competence and support. I am very grateful for the fun and productive teamwork and I am happy to know that the experiment is in his safe hands with its continuation. I also want to send my gratitude to the remaining optomechanics team: Luiz, Dennis, Daniel, Yinching, and with a special thank you to Angelo and Frederik. Furthermore, I would like to give a sincere thanks to Renato for his always calm and friendly help in the lab.

A warm thank you goes to a lot of colleagues along the way for their support in many different ways: Deepak, Maxime, Juanita, Josh, Lucca, Rasmus, and Iyad. You kept me floating. In particular, a special thank you to Rayssa and Anna, who have been invaluable support throughout my time in the group. A thank you to all in QPIT, who I didn't mention by name. I am grateful for all

the knowledge sharing, sparring, help and fun throughout the three years in the research group. Thank you to the workshop for always helping out when in need for new components to the experiment, as well as to our electronic engineer Aleksander Tchernavskij. A warm thank you to both Tine Hougaard Klitmøller and Vivi Schack Kempel for the administrative help and for always taking care of us in the group.

For my short external stay - due to the pandemic - I was lucky to get the chance to visit Michael Vanners research group at Imperial College London, and I want to thank him for his hospitality, generosity and for all the interesting physics discussions. I also want to thank DTU, the Physics Department, the Danish National Research Foundation, and all the tax-payers of Denmark to make it possible to devote three years of my life to this research.

Lastly a warm and heartfelt thank you to my family; mother, father, and brother, as well as to Jane, Friederikke, Kåre, to my collective; Amalie, Emil, Kristian, Sigurd, and Theresa, to Rune and to my friends, especially Manja and Louise, for supporting me each in their own unique way. I am so grateful and lucky to have them in my life.

Contents

Chapter 1

Introduction

Quantum mechanics has been a source of fascination since its foundation around a century ago, at the "first quantum revolution" established by many prominent figures in physics; Bohr, Einstein, Heisenberg, Dirac, just to mention a few. Now, a century later, the advances and high level of control of quantum measurements have paved the way for the currently ongoing "second quantum revolution" with development of quantum technology, such as the first quantum computers, predicted by Feynman in 1982 [1].

The theory of quantum mechanics describes nature on the very fundamental level and is, with its many facets, one of the most successful theories in the history of science. Nevertheless, questions remain unexplained, such as the quantum measurement problem - why quantum superpositions do not seem to occur on a macroscopic scale [2] and how quantum theory relates to the theory of general relativity [3], [4]. One way to approach these fundamental questions is through quantum optomechanics.

Quantum optomechanics is the interaction between light and (macroscopic) mechanical resonators on a quantum level. The interaction occurs via radiation pressure, which arises when photons carrying momentum are being reflected from an object. Such forces were postulated by Kepler already in 1619, long before the first quantum revolution, from observing the dust tails from comets, pointing away from the sun [5]. The statistics of the fluctuations from radiation pressure

force acting on a movable mirror was derived centuries later by Einstein in 1908 [6]. The first pioneering experiments demonstrating the effects of momentum transfer from photons onto atoms and crystal quartz plates were done in the 1930s [7], [8]. Another type of optomechanical interaction, different from radiation pressure, is Brillouin scattering, or Brillouin-Mandelstam scattering, which occurs via electrostriction. It was independently predicted by Brillouin in 1922 [9] and Mandelstam in 1926 [10] and experimentally verified by Gross in 1930 [11]. Since then, especially within the last decade, many advances have been made within optomechanics. Recently, entanglement has been demonstrated between two (similar) macroscopic objects [12], [13], [14], and between two different macroscopic objects [15], as well as quantum teleportation between two optomechanical devices [16].

Another beneficial feature of optomechanics is the capability of sensing with a very high sensitivity. At LIGO, gravitational waves were detected for the first time in 2016 [17], exactly 100 years after being predicted [18], [19], using very large (40 kg) optomechanical mirrors in a km sized interferometer.

Besides probing fundamental questions within physics, quantum optomechanics offers promising prospects for a variety of hybrid quantum technologies [20]. Usually in quantum experiments, phonons, the quantisation of vibrations, are a source of decoherence. But when controlled, they can be used as information carriers, for e.g. quantum memories [21], [22]. Furthermore, the frequency conversion in optomechanical devices can be used for transduction between the microwave and optical domain [23], [24]. These optomechanical devices may serve as highly promising candidates for creating links between super conducting quantum computers[25] in a future quantum internet [26].

To develop feasible hybrid quantum technology, the optomechanical system of interest is first of all required to operate in the quantum regime. For the mechanics to sustain long-lived coherent phonon modes, it is beneficial to optimise the Qf-product, where Q is the quality factor and f the frequency of the mechanics. Additionally, in order to obtain coherent state transfer between the optics and the mechanics (for e.g. quantum memories and transducers) strong coupling between the two respective modes is desirable and is thus an important achievement. In the optomechanics community, impressive work has been demonstrated with high quality resonators in the kHz and MHz range [27], [28], [29]. When approaching the quantum regime of the mechanics, it is advantageous to use mechanics with frequencies in the GHz range, as the quantum ground state will be accessible by cooling with standard bulk refrigerator techniques.

Coherent long-lived phononic modes in crystalline materials were demonstrated in the Rakich group at Yale [30]. The Brillouin response from crystalline quartz,

and other materials all in the GHz range, was investigated both at room temperature and at ~ 10 K, using plano-convex shaped crystalline materials, and thereby creating a phononic cavity. The same group also demonstrated optomechanically induced amplification and transparency at ~ 10 K for a flat-flat-faceted quartz crystal inside an optical cavity to enhance the coupling [31]. Recently, strong coupling between the optical and acoustic modes was demonstrated in the same system also at ~ 10 K [32].

Inspired by the above, the main objective of this work is to both combine a phononic cavity (plano-convex quartz crystal) and an optical cavity and cool the system to its quantum ground state at milli-Kelvin temperatures. Ground state operation of a cavity optomechanical system using bulk acoustic waves has until now not been demonstrated. This system with its high Qf-product, when in its ground state, will allow for coherent state transfer, thus enabling incredible applications; such as development of a quantum memory, tomography of single-phonon Fock states, or transfer of non-classical states (e.g. squeezed states [33] or cat states [34]) from the optics to the acoustics. In this thesis, a state-of-the-art design of a cryogenic cavity for ground state cooling and the first characterizations of the cavity are presented.

To first demonstrate the concept for room temperature operation, a similar optomechanical system consisting of a flat-flat-faceted quartz crystal inside a high finesse optical cavity was designed. For this optomechanical cavity, both Brillouin lasing and strong coupling between the acoustic and optical modes were achieved. Phonon lasing for a similar system was demonstrated in [31] but only for low temperatures, whereas Brillouin lasing occurs for broader acoustic linewidths at room temperature, and is the first time to be demonstrated for a system like this. Though strong coupling was recently demonstrated at room temperature in a micro resonator supporting whispering gallery modes [35] by Enzian et al, strong coupling is for the first time achieved in room temperature for an optomechanical cavity of this type, presented in this thesis.

The structure of this thesis is the following; first an introduction to cavity optomechanics and Brillouin scattering are presented in chapter 2. Subsequently, the simulations of the physical design criteria for the two optomechanical cavities are presented in chapter 3. The experimental design and observation of Brillouin lasing and strong coupling between the acoustic and optical mode at room temperatures are presented in chapter 4. Finally, a state-of-the-art design of the cryogenic cavity for ground state cooling and the first characterizations of the cavity are presented in chapter 5. The thesis is closing with a conclusion and prospects for future work in chapter 6.

Chapter 2

Theoretical Background

2.1 Introduction

In this chapter, a brief introduction to cavity optomechanics and Brillouin scattering is presented as well as a general overview of the theory used throughout the thesis.

2.2 Cavity Optomechanics

At its core, cavity optomechanics is the interaction between optics and mechanics, where the optical field, and therefore this interaction, is enhanced by an optical cavity. In optomechanical experiments, the mechanics can take many forms. Some examples are small membranes and trampolines visible to the naked eye [36], [27], micro resonators supporting whispering gallery modes [35], micro toroids [37], superfluid helium [38], phononic crystals [22], or bulk crystals supporting bulk acoustic waves [31]. In this section, a brief summary of cavity optomechanics is presented. An in-depth introduction to the field can be found in the review paper by Aspelmeyer et al. [39].

The canonical example of cavity optomechanics is a Fabry Pérot cavity with one mechanically compliant mirror on a spring, as shown in figure 2.1. The optical field, enhanced by the optical cavity, affects the displacement of the mirror by radiation pressure.

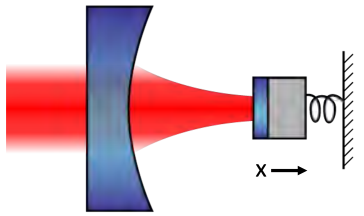

Figure 2.1: Canonical example of an optomechanical cavity; an optical field inside a Fabry Pérot cavity with one moving mirror on a spring. Figure adapted from [40].

The simple case of a single cavity mode and a single mechanical mode with the eigenfrequencies, ω_j and Ω_m, respectively is first considered. The Hamiltonian describing the uncoupled fields of the optics and mechanics is $\hat{H} = \hbar\omega_j\hat{a}^\dagger\hat{a} + \hbar\Omega_m\hat{b}^\dagger\hat{b}$, where $\hat{a}^\dagger$, $\hat{a}$ are the creation and annihilation operators for the optical mode and $\hat{b}^\dagger$, $\hat{b}$ are the creation and annihilation operators for the mechanical mode. Next, the interaction between the optics and mechanics is introduced, where the radiation pressure from the optical field affects the displacement of the mirror, and the displacement of the mirror affects the optical cavity field. Displacement of the mirror in the x-direction from its original position affects the frequency of the cavity field, which Taylor expanded to first order becomes, $\omega_j(x) \approx \omega_j + x\frac{\partial}{\partial x}(\omega_j) + ...$, thus the shift in frequency per displacement is $g = -\frac{\partial}{\partial x}(\omega_j)$. Using $x = x_{zpf}(b + b^\dagger)$, where $x_{zpf} = \sqrt{\hbar/(2m_{eff}\Omega_m)}$ is the zero point fluctuation, and m_{eff} is the effective mass of the resonator, the Hamiltonian takes the form,

$$\hat{H} = \hbar\omega_j\hat{a}^\dagger\hat{a} + \hbar\Omega_m\hat{b}^\dagger\hat{b} + \hbar g_0\hat{a}^\dagger\hat{a}(\hat{b} + \hat{b}^\dagger) \tag{2.1}$$

where the last term

$$\hat{H}_{int} = \hbar g_0\hat{a}^\dagger\hat{a}(\hat{b} + \hat{b}^\dagger) \tag{2.2}$$

represents the interaction between the optical and mechanical field. The parameter $g_0 = gx_{zpf}$ is the vacuum optomechanical coupling strength and

quantifies the coupling rate between a single photon and a single phonon [39].

The enhanced optomechanical coupling rate in the linearized regime (discussed in section 2.3) is $G = g_0\sqrt{\bar{N}_{cav}}$, where $\bar{N}_{cav}$ is the average number of photons in the cavity. Another important quantity in optomechanics, besides the eigenfrequencies of the optical and mechanical modes and the optomechanical coupling rate, is the dissipation (or decay) rate κ and Γ of the optical and mechanical modes, respectively. The dissipation rate is associated with the (incoherent) coupling of these modes to their respective environments.[1] A pictorial sketch of the key figures of merit for the coupled harmonic oscillators is shown in figure 2.2.

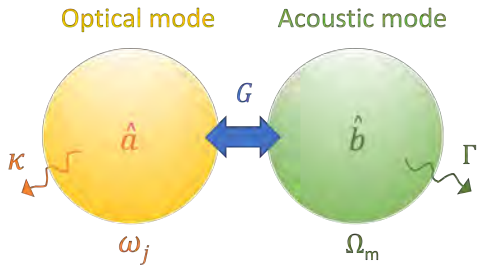

Figure 2.2: Pictogram of coupling, G, between the optical mode, $\hat{a}$, and the acoustic mode, $\hat{b}$, at the frequencies ω_j and Ω_m and with dissipation rates κ and Γ for the the optical and acoustic modes respectively.

When the cavity decay rate, κ, is much larger than the mechanical frequency Ω_m, it is known as the unresolved cavity or "bad cavity" regime. In this regime, the optical field can probe and change the state of the mechanics, used for e.g. mechanical feedback cooling [27]. On the other hand when the mechanical frequency is much lager than the optical decay rate, $\Omega_m \gg \kappa$, the optomechanincal interaction takes place in the resolved sideband regime. For this work, only the resolved sideband regime is considered. Furthermore, the interaction Hamiltonian can be transformed into a beam-splitter or a two-mode squeezing Hamiltonian in the resolved sideband regime (discussed in section 2.3).

Other key figures of merit for an optomechanical cavity is the finesse of the optical system, $\mathcal{F} = \mathrm{FSR}/\kappa$, where the free spectral range FSR is the mode spacing between the fundamental cavity modes in frequency domain. For the mechanics, a good way to evaluate its performance is by comparing its frequency

[1] Linewidth, dissipation rate, damping rate, and decay rate will be used interchangeably throughout the thesis, where the convention of full width half maximum (FWHM) is used.

to the decoherence rate, given by the quality factor $Q = \Omega_m/\Gamma$. The number of coherent oscillations for a given resonator is proportional to the $Q \cdot f$ product, where $f = \Omega_m/2\pi$ is the frequency. When approaching the quantum regime of the mechanics, it is of high interest to know the average phonon number in thermal equilibrium $\bar{n}_{th} = 1/(e^{\hbar\Omega_m/k_BT} - 1)$, given by the Planck distribution [41], revealing how close the mechanics is to be in its quantum ground state.

2.3 Stokes and anti-Stokes Interaction

From the interaction Hamiltonian in equation 2.2, it follows that the interaction is fundamentally a nonlinear process. When linearising the Hamiltonian, using $\hat{a} = \bar{\alpha} + \delta\hat{a}$, where $\bar{\alpha} = \langle a \rangle$ is the coherent amplitude of the optical field and $\delta\hat{a}$ is the fluctuating term of the optical field, the interaction Hamiltonian becomes [39]:

$$\hat{H}_{int}^{(lin)} = -\hbar G(\delta\hat{a}^\dagger + \delta\hat{a})(\hat{b} + \hat{b}^\dagger) \tag{2.3}$$

where the effective optomechanical coupling is $G = g_0\sqrt{\bar{N}_{cav}}$. Detuning of a laser pump (or a sideband created from the pump) is tuning the frequency of the pump slightly off the frequency of the cavity mode of interest. Depending on the detuning, there are different regimes of relevance. Here, considering the resolved sideband regime and keeping only the resonant terms, using the rotating-wave approximation, one can arrive at the "beam-splitter" (BS) Hamiltonian and the "two-mode squeezing" (TMS) Hamiltonian:

$$\hat{H}_{BS} \propto \delta\hat{a}^\dagger\hat{b} + \hat{b}^\dagger\delta\hat{a} \tag{2.4}$$

$$\hat{H}_{TMS} \propto \delta\hat{a}^\dagger\hat{b}^\dagger + \hat{b}\delta\hat{a} \tag{2.5}$$

The beam-splitter Hamiltonian, $\hat{H}_{BS}$, resembles the anti-Stokes process, sketched in figure 2.3. Here, considering only one optical mode, the laser pump is red-detuned from the cavity mode. The sidebands are at the same frequency as the mechanical frequency, Ω_m. The blue-detuned sideband is resonant with the cavity mode and thus the anti-Stokes process is amplified. The opposite interaction, the Stokes process described by the two-mode squeezing Hamiltonian, $\hat{H}_{TMS}$, is suppressed, since the red-detuned sideband is out of resonance.

Beam-splitter interaction, or anti-Stokes process, corresponds to annihilating a photon from the pump field and a phonon from the mechanical mode and creating a photon of higher frequency in the cavity mode, thereby cooling the mechanical mode. The two-mode squeezing interaction, or the Stokes process, corresponds to an annihilation of a photon from the pump field and creation of a phonon in the mechanical mode and a lower frequency photon in the cavity field, thus heating of the mechanical mode. An energy diagram of the two processes are shown in figure 2.4c.

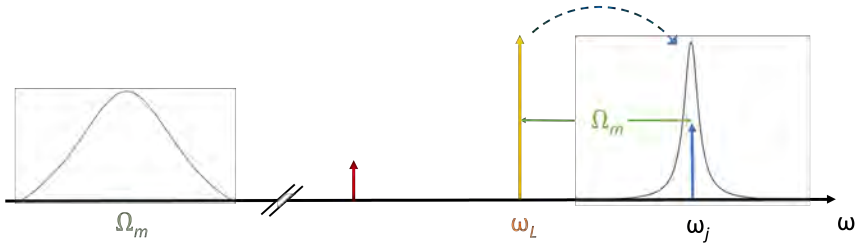

Figure 2.3: Sideband cooling of the optical cavity mode. The sidebands are at the same frequency as the mechanical frequency, Ω_m. The blue-detuned sideband is resonant with the cavity mode, while the red-detuned sideband is not, thus the anti-stokes process is amplified while the Stokes process is suppressed.

Usually in cavity optomechanics, a single cavity mode is considered. For this work two cavity modes are regarded, where also the laser pump mode is resonant in addition to the mechanical mode. By probing either the red-detuned mode or the blue-detuned mode in respect to the control laser, either a Stokes or anti-Stokes process is probed. If the probe, aka the sideband, is red-detuned from the pump, the Stokes process is stimulated, as in figure 2.4a. If on the other hand, the probe is blue-detuned from the pump, and both the pump and probe are resonant with the cavity modes, the anti-Stokes process is stimulated, as in figure 2.4b. If the mode spacing is symmetrical, the two processes will be stimulated at the same time. In chapter 3, the advantages of an asymmetric mode spacing, will be discussed further.

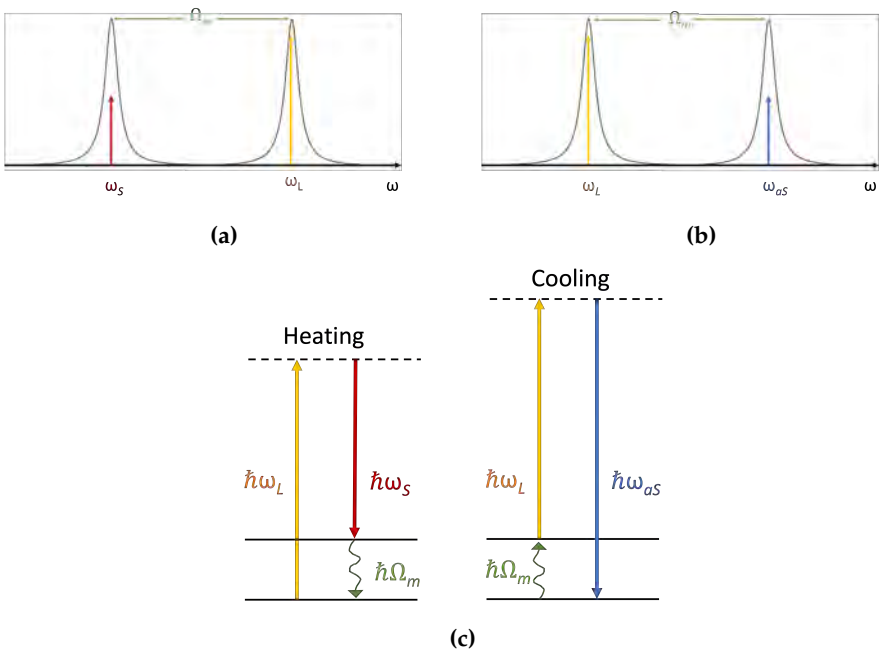

Figure 2.4: **(a)** Stokes process where the mode spacing between the cavity modes matches the Brillouin frequency, Ω_m, and the pump at ω_l is resonant with the blue-detuned mode and the probe is resonant with the red-detuned mode at ω_S. **(b)** Anti-Stokes process where the mode spacing between the cavity modes matches the Brillouin frequency, Ω_m, and the pump at ω_l is resonant with the red-detuned mode and the probe is resonant with the blue-detuned mode at ω_{aS}. **(c)** Energy diagram of the two processes.

2.4 Brillouin Scattering

Brillouin scattering is an optomechanical interaction different from radiation pressure, and stems from inelastic scattering of light from elastic waves, and on a quantum level, from acoustic phonons. Brillouin scattering occurs via electrostriction, a tendency of materials to become more dense under the influence of an electric field. It is an optomechanical coupling between the optical field and the local displacement of the (macroscopic) dielectric medium, where the local compression and expansion of the material correspond to the longitudinal acoustic pressure waves. Unlike other optomechanical interactions, Brillouin scattering is a bulk effect, where the defining feature is the ratio of the speed of sound to the speed of light in the material [42].

Brillouin scattering is a three wave mixing interaction and can arise from either a Stokes or an anti-Stokes process. In a Stokes process, a photon from the incident laser pump field at frequency, ω_l, is converted into a lower frequency Stokes photon at frequency ω_S and an acoustic phonon at frequency, Ω_m in the inelastic scattering process, where $\omega_l = \omega_S + \Omega_m$, shown in figure 2.5a. On the other hand, a photon from the laser field can also absorb the energy of an acoustic phonon and produce a high frequency anti-Stokes photon at frequency, $\omega_{aS} = \omega_l + \Omega_m$, as shown in figure 2.5b. In this thesis, Brillouin scattering in crystalline quartz is studied, where Stokes (and anti-Stokes) waves propagate opposite to the laser pump, known as backward Brillouin scattering. The acoustic wave propagates in the same direction as the laser pump in Stokes scattering (see figure 2.5c) and opposite for the anti-Stokes scattering.

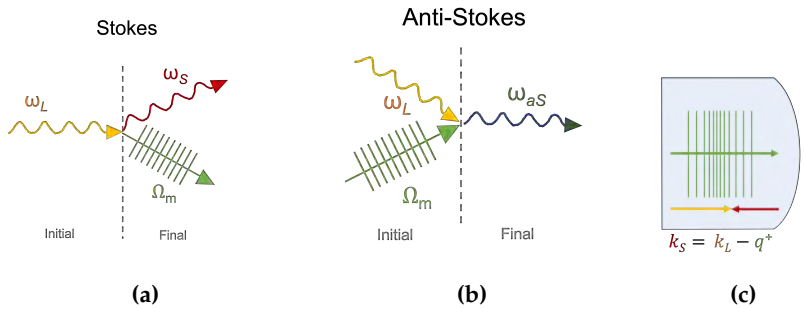

Figure 2.5: **(a)** A Stokes process, where a photon from the laser pump field at frequency, ω_l is downshifted to a Stokes photon with lower frequency, ω_S, and an acoustic phonon at frequency, Ω_m. **(b)** An anti-Stokes process, where a photon from the laser pump field absorbs the energy of an acoustic phonon at frequency Ω_m, and gets up-shifted to an anti-Stokes photon at higher frequency, ω_{aS}. **(c)** Sketch of the wave-vectors in a Stokes process in crystalline quartz. The acoustic wave-vector, q^+, is propagating in the same direction as the wave-vector for the pump field, k_l. The wave-vector for the Stokes field, k_S is propagating in opposite direction (Backward Brillouin scattering).

To obtain resonant energy transfer, energy conservation and phase matching must be satisfied: $\hbar\omega_S = \hbar\omega_l - \hbar\Omega_m$ and $\mathbf{k}(\omega_S) = \mathbf{k}(\omega_l) - \mathbf{q}^-(\Omega_m)$ (Stokes process), where the general relation between the rotational frequency, ω, and the wave-vector, $\mathbf{k}$, is $\omega = |\mathbf{k}|c/n$ and for the acoustics $\Omega_m = |\mathbf{q}|v_a$ [43]. For a backward propagating acoustic wave in an anti-Stokes process the dispersion relation is $\mathbf{k}(\omega_{aS}) = \mathbf{k}(\omega_l) + \mathbf{q}^+(\Omega_m)$. From these requirements the Brillouin frequency, Ω_m, can be calculated [30]:

$$\Omega_m = \frac{2\omega_l v_a/v_o}{1 \pm v_a/v_o} \approx 2\omega_l v_a/v_o \tag{2.6}$$

where ω_l is the frequency of the laser pump and v_a (v_o) is the speed of sound (light) in the given material. The plus-sign in the denominator is for the Stokes process, and the minus-sign for the anti-Stokes process, where $v_o \gg v_a$ is used for the approximation [43].

To ensure that the scattering amplitudes from different regions constructively interfere, phase matching must be maintained between the three waves that take part in the interaction, meaning that they have a specific phase relationship throughout the interaction region [44], [42]. The dispersion relation, which links the angular frequency, ω, and wave-vector, $\mathbf{k}$, of an elastic wave, provides insight into its propagation behaviour. In figure 2.6 the dispersion relation of the optics and acoustics is shown.

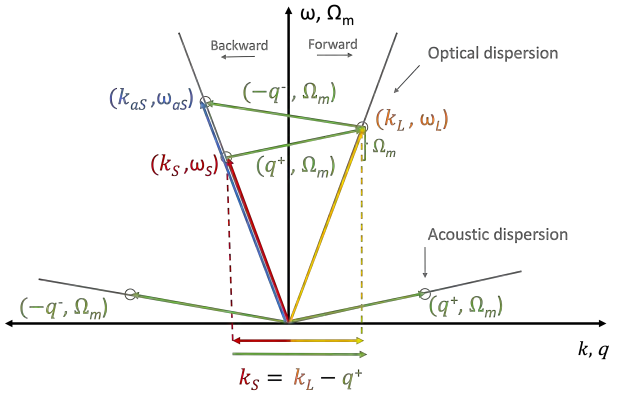

Figure 2.6: Sketch of the acoustic and optical dispersion diagram for backward Brillouin scattering of both a Stokes and anti-Stokes process, displaying the relations between the frequencies, ω_i, Ω_m and the wave-vectors $\mathbf{k_i}, \mathbf{q}$.

2.4.1 Brillouin Lasing

In a Stokes process, the beating between the laser pump and the acoustic wave tends to reinforce the Stokes field, while the beating between the laser pump and the Stokes wave reinforces the acoustic wave. The two processes can under the right conditions build up a positive feedback, such that the Brillouin gain,

g_{sbs}, exceeds the round trip losses and amplifies exponentially, also known as Brillouin lasing. Brillouin lasing was first experimentally demonstrated in 1964 [45]. The threshold power, P_{th}, of Brillouin lasing is approximately [46]:

$$P_{th} \simeq \frac{\pi^2 n^2 V \kappa_l \kappa_S}{c^2 g_{sbs}} \tag{2.7}$$

where n is the refractive index, V is the mode volume, κ_l is the linewidth of the laser pump, κ_S is the linewidth of the Stokes field. c is the speed of light in vacuum and g_{sbs} is the Brillouin gain, derived in [47]:

$$g_{sbs}(\Omega) = \tilde{g}_0 \frac{(\Gamma/2)^2}{(\Omega_m - \Omega)^2 + \Gamma/2)^2} \tag{2.8}$$

where Γ is the acoustic dissipation rate and Ω_m is the Brillouin frequency. $\Omega = \omega_l - \omega_S$ is the frequency detuning, and

$$\tilde{g}_0 = \frac{\omega^2 n^7 p_{13}^2}{c^3 v_a \rho \Gamma A} \tag{2.9}$$

is the peak Brillouin gain (or line-center gain factor) measured in $[\tilde{g}_0] = \mathrm{m}^{-1}\mathrm{W}^{-1}$. The optical frequencies $\omega_l \simeq \omega_S = \omega$, and p_{13} is the relevant elasto-optic constant. v_a is the speed of sound in the material, ρ is the density, and A is the common mode area of the acoustic and optical field.

2.5 Optomechanically Induced Transparency

Optomechanically induced transparency (OMIT) is a cavity optomechanical phenomenon similar to Electromagnetically induced transparency (EIT) in atomic systems. The process stems from an interference that produces a cancellation of the intra-cavity field, that gives rise to a transparency window. In the weak coupling regime $G \ll \{\kappa, \Gamma\}$, for a decay rate hierarchy, $\Gamma \ll \kappa$, a narrow dip in the transmission spectrum appears. For the opposite decay rate hierarchy $\Gamma \gg \kappa$, the OMIT dip is not resolvable but the interaction can affect the shape of the optical linewidth slightly. In the strong coupling regime, $G > \frac{\kappa+\Gamma}{2}$, for both decay rate hierarchies, the optical transmission spectrum transforms

into two resonant modes originating from the hybridisation between the optical and the mechanical mode [39], [48].

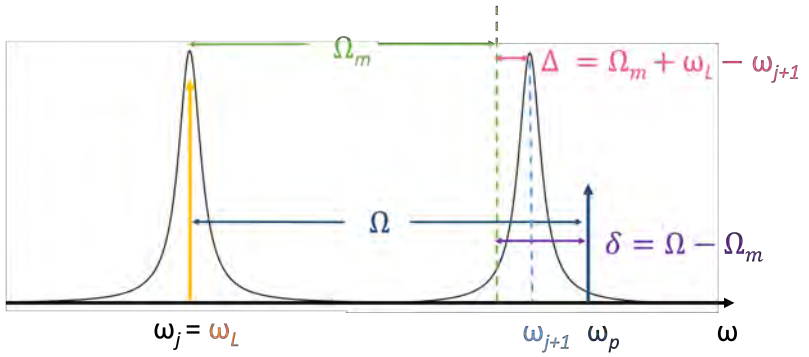

Figure 2.7: Sketch of an OMIT measurement. A strong red detuned laser pump at frequency ω_l is resonant with the lower frequency cavity mode, while a weak probe at frequency ω_p is sweeping over the higher frequency cavity mode at $\omega_{(j+1)}$. Δ is the optical cavity detuning from the Brillouin frequency Ω_m and δ it the detuning of the probe from the Brillouin frequency.

In figure 2.7 a sketch of an OMIT interaction is shown. Here, a strong laser field at frequency, ω_l, is on resonance with the low frequency cavity mode at ω_j. A weak blue-detuned sideband probe at frequency, ω_p, is sweeping over the high frequency cavity mode at $\omega_{(j+1)}$, stimulating the anti-Stokes process. The FSR $= \omega_{(j+1)} - \omega_j$ is slightly detuned from the Brillouin frequency, Ω_m, denoted by $\Delta = \Omega_m + \omega_l - \omega_{(j+1)} = \Omega_m - \mathrm{FSR_j} = \Omega_m - (\omega_{(j+1)} - \omega_j)$. The detuning of the probe, ω_p in respect to the Brillouin response is denoted by $\delta = \Omega - \Omega_m = \omega_p - \omega_l - \Omega_m$.

The full Hamiltonian of the optomechanical cavity is, following the derivation in [49]:

$$\hat{H} = \hat{H}_0 + \hat{H}_{int} + \hat{H}_{drive} \tag{2.10}$$

where

$$\begin{aligned}\hat{H}_0 &= \hbar\omega_j\hat{a}_j^\dagger\hat{a}_j + \omega_{(j+1)}\hat{a}_{(j+1)}^\dagger\hat{a}_{(j+1)} + \hbar\Omega_m\hat{b}^\dagger\hat{b}\\ \hat{H}_{int} &= -\hbar g_0\left(\hat{a}_{(j+1)}^\dagger\hat{a}_j\hat{b} + \hat{b}^\dagger\hat{a}_j^\dagger\hat{a}_{(j+1)}\right)\\ \hat{H}_{drive} &= i\hbar\sqrt{\kappa_j^{\text{ext}}}\alpha_l\left(\hat{a}_j^\dagger e^{-i\omega_l t} - \hat{a}_j e^{i\omega_l t}\right)\\ &\quad + i\hbar\sqrt{\kappa_{(j+1)}^{\text{ext}}}\alpha_p\left(\hat{a}_{(j+1)}^\dagger e^{-i\omega_p t} - \hat{a}_{(j+1)}e^{i\omega_p t}\right)\end{aligned} \tag{2.11}$$

Assuming a strong laser field pumping the cavity mode, $\hat{a}_j$, the undepleted pump approximation can be applied and the field can be treated classically:

$$\langle\hat{a}_j\rangle = \sqrt{N_j}e^{-i\omega_l t} \tag{2.12}$$

where N_j is the laser driven intra-cavity photon number for the mode $\hat{a}_j$. The expression for $\langle\hat{a}_j\rangle$ is then inserted, to linearise the interaction Hamiltonian:

$$\hat{H}_{int} = -\hbar g_0\sqrt{N_j}\left(\hat{a}_{(j+1)}^\dagger\hat{b}e^{-i\omega_l t} + \hat{b}^\dagger\hat{a}_{(j+1)}e^{i\omega_l t}\right) \tag{2.13}$$

Using the rotating wave approximation with $\hat{a}_{(j+1)}(t) \rightarrow \hat{a}_{(j+1)}(t)e^{-i\omega_p t}$ followed by $\hat{b}(t) \rightarrow \hat{b}(t)e^{i(\omega_l-\omega_p)t}$ the interaction Hamiltonian takes the form,

$$\hat{H}_{int} = -\hbar G\left(\hat{a}_{(j+1)}^\dagger\hat{b} + \hat{b}^\dagger\hat{a}_{(j+1)}\right) \tag{2.14}$$

Now, with these assumptions the effective Hamiltonian becomes:

$$\begin{aligned}\hat{H}_{eff} &= -\hbar\delta\hat{b}^\dagger\hat{b} - \hbar\Big(\delta+\Delta\Big)\hat{a}_{(j+1)}^\dagger\hat{a}_{(j+1)} - \hbar G\left(\hat{a}_{(j+1)}^\dagger\hat{b} + \hat{b}^\dagger\hat{a}_{(j+1)}\right)\\ &\quad + i\hbar\sqrt{\kappa_{(j+1)}^{ex}}\alpha_p\left(\hat{a}_{(j+1)}^\dagger - \hat{a}_{(j+1)}\right)\end{aligned} \tag{2.15}$$

where $\delta = \Omega - \Omega_m = \omega_p - \omega_l - \Omega_m$ is the detuning of the probe in respect to the Brillouin response. $\Delta = \Omega_m + \omega_l - \omega_{(j+1)}$ is the detuning of the FSR $(\omega_{(j+1)} - \omega_j)$ with respect to the Brillouin frequency, Ω_m.

Deriving the Heisenberg equation of motion from the effective Hamiltonian, yields:

$$\begin{aligned}\frac{d}{dt}\hat{b}(t) &= \Big(i\delta - \frac{\Gamma}{2}\Big)\hat{b} + iG\hat{a}_{(j+1)} \\ \frac{d}{dt}\hat{a}_{(j+1)}(t) &= \Big(i(\delta+\Delta) - \frac{\kappa_{(j+1)}}{2}\Big)\hat{a}_{(j+1)} + iG\hat{b} + \sqrt{\kappa^{ex}_{(j+1)}}\alpha_p\end{aligned} \tag{2.16}$$

where Γ is the dissipation rate of the mechanical mode, and the optical dissipation rate is $\kappa = \kappa_{ex} + \kappa_0$. κ_{ex} is the loss rate related to the input coupling and κ_0 is the intrinsic loss rate. $\kappa_{ex} = T/\tau$ where T is the transmission of the first mirror and $\tau = 2L/c$ is the round-trip time of light in the cavity [50]. From the equation of motion, the steady state of $\hat{b}$ and $\hat{a}_{(j+1)}$ can be found:

$$\begin{aligned}\hat{b} &= \frac{-iG}{(i\delta - \Gamma/2)}\hat{a}_{(j+1)} \\ \hat{a}_{(j+1)} &= \frac{-\sqrt{\kappa^{ex}_{(j+1)}}\alpha_p}{i(\delta+\Delta) - \frac{\kappa_{(j+1)}}{2} + \frac{G^2}{i\delta - \Gamma/2}}\end{aligned} \tag{2.17}$$

Using the input-output formalism, an expression for the transmitted probe light is obtained,

$$\hat{a}_{(j+1)out} = \sqrt{\kappa^{ex}_{(j+1)}}\hat{a}_{(j+1)} = \frac{-\kappa^{ex}_{(j+1)}}{i(\delta+\Delta) - \frac{\kappa_{(j+1)}}{2} + \frac{G^2}{i\delta - \Gamma/2}} \tag{2.18}$$

Conclusively, the measure of interest is the power spectrum, which can be measured by heterodyne detection. For the transmission, the power spectrum follows:

$$P_T(\delta) \propto \langle \hat{a}^{\dagger}_{(j+1)out}\hat{a}_{(j+1)out}\rangle = \left|\frac{\kappa^{ex}_{(j+1)}}{i(\delta+\Delta) - \frac{\kappa_{(j+1)}}{2} + \frac{G^2}{i\delta - \Gamma/2}}\right|^2 \tag{2.19}$$

which is of great importance for the result section in chapter 4.

2.6 Strong Coupling Regime

The strong coupling regime is of key interest in quantum optomechanics, motivated in chapter 1, and was first experimentally demonstrated for a micromechanical resonator in 2009 [51]. Strong coupling can occur when the coupling between the optical and mechanical mode exceeds the total dissipation rate. The coupling rate quantifies the strength with which the optical and mechanical fields coherently exchange energy. Strong coupling can be reached by enabling the anti-Stokes process, described by the beam-splitter Hamiltonian. Considering only the non-dissipative terms of H_{eff}, in equation (2.15) in the case of the optical detuning, $\Delta = 0$, where the FSR match the Brillouin frequency, the expression becomes:

$$\hat{H}_{eff}(\Delta = 0) = -\hbar\delta\hat{b}^{\dagger}\hat{b} - \hbar\delta\hat{a}^{\dagger}_{(j+1)}\hat{a}_{(j+1)} - \hbar G\left(\hat{a}^{\dagger}_{(j+1)}\hat{b} + \hat{b}^{\dagger}\hat{a}_{(j+1)}\right) \tag{2.20}$$

The Hamiltonian can be diagonalised using the normal modes $\hat{c} = \frac{1}{\sqrt{2}}\left(\hat{a}_{(j+1)} + \hat{b}\right)$ and $\hat{d} = \frac{1}{\sqrt{2}}\left(\hat{a}_{(j+1)} - \hat{b}\right)$ yielding [48]:

$$\hat{H} = -\hbar(\delta + G)\hat{c}^{\dagger}\hat{c} - \hbar(\delta - G)\hat{d}^{\dagger}\hat{d} \tag{2.21}$$

From this expression it can be extracted that the coupling, G, between the hybrid modes, $\hat{c}$ and $\hat{d}$, results in a frequency splitting of $2G$.

For the light-enhanced optomechanical coupling for the linearised regime, $G = g_0\sqrt{\bar{N}_{cav}}$, the average number of photons, $\bar{N}_{cav}$, in cavity mode, $\hat{a}_{(j+1)}$ is given by [39]:

$$\bar{N}_{cav} = |\langle\hat{a}_{(j+1)}\rangle|^2 = \frac{\kappa^{ex}_{(j+1)}}{\Delta_l^2 + (\kappa_{(j+1)}/2)^2}\frac{P_{in}}{\hbar\omega_l} \tag{2.22}$$

where P_{in} is the input power and $\Delta_l = \omega_l - \omega_j$ is the detuning of the laser pump, ω_l, with respect to the cavity mode, ω_j (not to be confused with Δ).

For a z-cut crystal, the single photon coupling rate, g_0, can be approximated (order of magnitude) to [47]

$$g_0 \approx \frac{\omega_j^2 n^3 p_{13}}{2c} \sqrt{\frac{\hbar}{\Omega_m \rho A L_{cr}}} \left(\frac{L_{cr}}{L_{cav}} \right) \tag{2.23}$$

where ω_j is the frequency of the optical cavity mode, n is the refractive index, and p_{13} is the relevant elasto-optic constant. The density is denoted by ρ, A is the common mode area of the acoustic and optical field, and L_{cr} (L_{cav}) is the length of the crystal (optical cavity).

In order to reach the strong coupling regime, the optomechanical coupling, G, must be greater than the effective decay rate of the hybrid optomechanical mode, [35]:

$$G > \frac{\kappa + \Gamma}{2} \tag{2.24}$$

When the optomechanical coupling also exceeds the thermal decoherence rate, $\bar{n}_{th}\Gamma$, so the coupling becomes

$$G > \frac{\kappa + \bar{n}_{th}\Gamma}{2} \tag{2.25}$$

the optomechanical system enters the quantum-coherent coupling regime and the interaction becomes quantum coherent. The coupling rate between the optics and mechanics is thus much faster than the decoherence of the quantum states. This criterion is of high importance for the successful implementation of many quantum protocols, such as quantum-state transfer between the cavity field and a mechanical mode [39], and has been experimentally demonstrated by different groups, for example in reference [37].

Chapter 3

System and Design Considerations

3.1 Introduction

In this chapter, the general physical criteria and the design considerations of the optomechanical system are presented.

The optomechanical system studied for this work, consists of a high finesse optical Fabry Pérot cavity with a quartz crystal inside, designed to operate at telecom wavelengths, $\lambda \sim 1550$ nm. Two different configurations are developed in this work; one for operation at milli-Kelvin temperatures, the other for operation at room temperature. The general physical considerations for both optomechanical systems are presented in this chapter. The optomechanical cavity designed to operate at milli-Kelvin temperatures consists of a high finesse optical cavity with a flat-curved-faceted quartz crystal inside, a schematic is shown in figure 3.1b. At milli-Kelvin temperatures, the coherence length of the phonons is much longer than the crystal length, $l_{ph} \gg L_{cr}$, and with the curvature of the crystal surface, the crystal itself can function as a phononic cavity. The final design of this configuration is presented in chapter 5. The optomechanical cavity designed to operate at room temperature is the same high finesse optical cavity, but with a flat-flat-faceted quartz crystal inside, a schematic is shown in figure 3.1a. The coherence length of the phonons in the

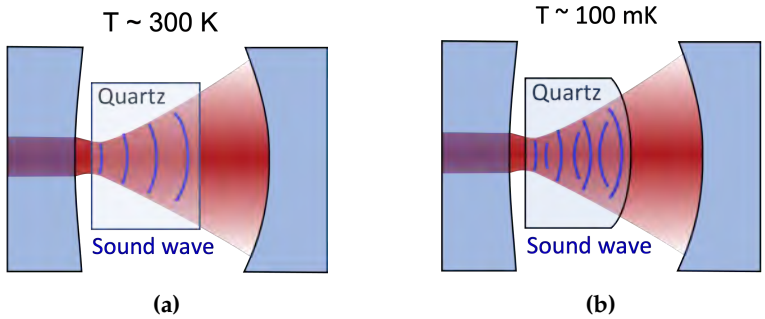

(a) (b)

Figure 3.1: The two different optomechanical cavities, studied for this work. Both are high finesse optical cavities with a cavity length of approximately 10 mm, both with a 4 mm long z-cut quartz crystal inside, one with a flat-flat-faceted surface for operation at room temperature **(a)**, the other with a flat-curved-faceted surface for operation at milli-Kelvin temperatures **(b)**.

crystal at room temperature is orders of magnitudes smaller than the length of the crystal, $l_{ph} \ll L_{cr}$, and thus not possible to obtain a phononic cavity at these scales and temperatures. Furthermore, it is much easier to align the optical beam using a flat-flat-faceted crystal than a curved-faceted one, hence the choice of crystal shape. The actual design of this configuration is presented at the end of this chapter.

3.2 Asymmetric Optical Mode Spacing

For a standard Fabry Pérot cavity in vacuum, the standing wave cavity modes are separated by the same free spectral range (FSR), determined by the speed of light, c, and the length, L_{cav}, of the optical path in the cavity, FSR $= c/(2L_{cav})$. If a medium of refractive index, n, is placed in between the mirrors, the optical mode spectrum can change radically. With a medium inside the cavity, the path of the propagating light increases which causes a decrease of the FSR. The medium of interest in this case is z-cut crystalline quartz, but can easily be replaced with other materials of interest, such as KTP or TeO_2. The reflection of the quartz crystal ($\sim 4\%$) contributes to several coupled cavities within the optomechanical system, as sketched in figure 3.2.

To model the optical mode spectrum of the coupled cavities, the transfer-

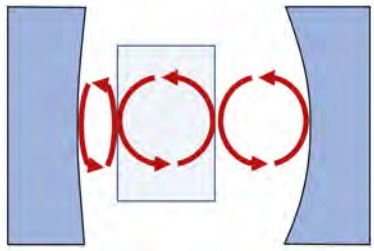

Figure 3.2: Schematics of the optical cavity with the quartz crystal inside, where the reflection of the crystal surface contributes to several coupled cavities.

matrix method is used [52]. The electric field, propagating in the z-direction is represented as a superposition between the right and left travelling wave: $E(z) = Ae^{-ikz} + Be^{ikz}$, where A and B are the amplitudes of the right- and left-travelling wave respectively. The electric field transforms under propagation, described by the transmission matrix, $\mathcal{T}$:

$$\begin{bmatrix} A_1 \\ B_1 \end{bmatrix} = \mathcal{T} \begin{bmatrix} A_2 \\ B_2 \end{bmatrix} \tag{3.1}$$

where 1 represents the electric field on the left side of the cavity and 2, the electric field on right side of the cavity. The full transmission matrix takes the form:

$$\mathcal{T} = \mathcal{T}_{mirror,1} \cdot \mathcal{T}_{vacuum,1} \cdot \mathcal{T}_{quartz} \cdot \mathcal{T}_{vacuum,2} \cdot \mathcal{T}_{mirror,2} \tag{3.2}$$

where

$$\mathcal{T}_{mirror,j} = \frac{1}{\sqrt{T_j}} \begin{bmatrix} 1 & \sqrt{R_j} \\ \sqrt{R_j} & 1 \end{bmatrix}, \quad \mathcal{T}_{vacuum,j} = \begin{bmatrix} e^{i\phi_j} & 0 \\ 0 & e^{-i\phi_j} \end{bmatrix} \tag{3.3}$$

Here ϕ is the phase acquired after propagation, $\phi = kz = 2\pi z/\lambda$. T is the transmission and R the reflection, with the relation $R + T = 1$, and $j = \{1, 2\}$. The mirrors are assumed to be lossless. For the first mirror the transmission is $T_{mirror,1} = 500$ ppm and the transmission is $T_{mirror,2} = 40$ ppm for the second mirror. $\mathcal{T}_{quartz}$ combines the interfaces between vacuum and quartz and the propagation within the quartz:

$$\begin{aligned}\mathcal{T}_{quartz} &= \mathcal{T}_{mirrorQuartz,1} \cdot \mathcal{T}_{propQuartz} \cdot \mathcal{T}_{mirrorQuartz,2} \\ &= \frac{1}{2}\begin{bmatrix} 1+n & 1-n \\ 1-n & 1+n \end{bmatrix} \cdot \begin{bmatrix} e^{i\phi_{cr}} & 0 \\ 0 & e^{-i\phi_{cr}} \end{bmatrix} \cdot \frac{1}{2n}\begin{bmatrix} n+1 & n-1 \\ n-1 & n+1 \end{bmatrix}\end{aligned} \tag{3.4}$$

The phase acquired by propagating the distance, $d_{vacuum,1} = d_{cr}$, between the first mirror and the crystal is $\phi_1 = 2\pi d_{cr}/\lambda$. The phase acquired from propagation in the crystal is $\phi_{cr} = 2\pi n L_{cr}/\lambda$, where L_{cr} is the length of the crystal. For the second distance in vacuum, $d_{vacuum,2} = L_{cav} - d_{cr} - L_{cr}$, the distance between the crystal and the second mirror, the phase acquired is $\phi_2 = 2\pi(L_{cav} - d_{cr} - L_{cr})/\lambda$.

The total reflection, R_{tot}, and transmission, T_{tot}, can be found by the matrix elements of the total transmission matrix [52]:

$$R_{tot} = \left|\frac{\mathcal{T}_{21}}{\mathcal{T}_{11}}\right|^2, \quad T_{tot} = \left|\frac{1}{\mathcal{T}_{11}}\right|^2 \tag{3.5}$$

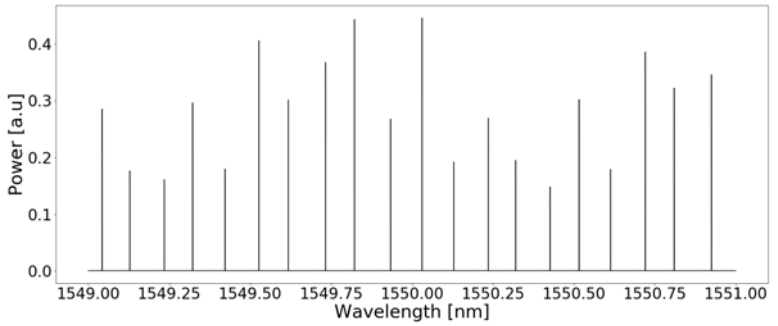

Figure 3.3: Simulations of a wavelength scan between 1549 nm – 1551 nm corresponding to the frequencies 193.3 THz – 193.6 THz, with the transmission shown in black. The plot displays the asymmetry of both the free spectral range and the asymmetry of the intensity of each mode.

In figure 3.3 the simulated optical power transmitted from the cavity is shown for the wavelengths 1549 nm – 1551 nm. Here the optical mode spectrum displays both the asymmetry of the free spectral range (FSR) and the intensity of the modes. Furthermore, there is also an asymmetry in the optical linewidths of the cavity mode, not visible in this figure. This simulation is made for a cavity length, $L_{cav} = 10$ mm with a crystal position, $d_{cr} = 1$ mm, and a crystal length

of L_{cr} = 4 mm. The rationales behind these choices, is unfolded later in this chapter. For this simulation, the variation of the FSRs is as large as ~ 20% with a reflectivity of the quartz of only ~ 4%. The asymmetry of the FSR spectrum comes with the advantage that the Hamiltonian of the system can be controlled, (as described in chapter 2), such that either the Stokes process is resonant with the Brillouin frequency, Ω_m, and the anti-Stokes process is suppressed, as in figure 3.4a, or such that the anti-Stokes process is resonant with the Brillouin frequency and the Stokes process is suppressed, as in figure 3.4b.

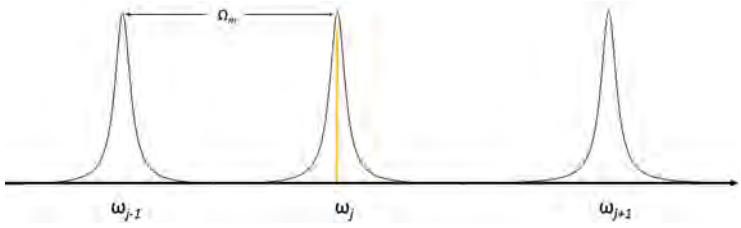

(a) Stokes process with the FSR = $\omega_j - \omega_{j-1}$ resonant with the Brillouin frequency, Ω_m, while the anti-Stokes process is suppressed.

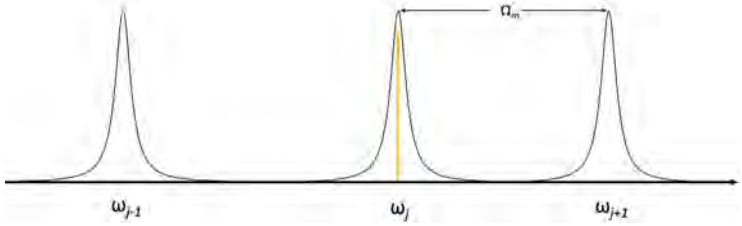

(b) Anti-Stokes process with the FSR = $\omega_{j+1} - \omega_j$ resonant with the Brillouin frequency, Ω_m, while the Stokes process is suppressed.

Figure 3.4: Stokes (a) and anti-Stokes (b) processes resonant with the Brillouin frequency Ω_m, while the opposite process is suppressed, due to the asymmetric FSR-spectrum. In both cases, the laser pump, represented by the yellow arrow, is resonant with the cavity mode ω_j.

3.3 Brillouin Scattering in Quartz

Brillouin scattering, which is a three wave mixing process between the photons and phonons in the crystal, requires energy conservation and phase matching conditions, $\omega_l = \omega_S + \Omega_m$ and $\mathbf{k}(\omega_l) = \mathbf{k}(\omega_S) + \mathbf{q}(\Omega_m)$, as described in further detail in chapter 2.

The Brillouin frequency, Ω_m, in a material is dependent on the laser pump

frequency, ω_l, the speed of sound in the material, v_a, and the speed of light in the material, v_0 [30]:

$$\Omega_m = \frac{2\omega_l v_a/v_o}{1 + v_a/v_o} \approx 2\omega_l v_a/v_o \tag{3.6}$$

The speed of sound in the longitudinal direction is $v_a = \sqrt{c_{33}/\rho}$, where $\rho = 2650$ kg/m^3 is the density, and $c_{33} = 106.1 \cdot 10^9$ Nm^{-2} is the relevant elastic constant. The speed of light in a given material, $v_0 = c/n$, depends on the speed of light in vacuum, c, and the refractive index, n. The refractive index depends both on the pump wavelength and the temperature, and is found using the Sellmeier formula [53]. At a pump wavelength, $\lambda = 1550$ nm, the refractive index for z-cut quarts is $n = 1.523$ at $T = 100$ mK and $n = 1.528$ at room temperature.

The Brillouin frequency for crystalline z-cut quartz is calculated for wavelength $\lambda = 1550$ nm to $\Omega_m = 12.47$ GHz at room temperature and $\Omega_m = 12.43$ GHz at 100 mK.

3.4 Cavity Design Criteria

In this section the different cavity design criteria; stability of the cavity, waist overlap of the optical and acoustic beam, and the optimal FSR spectrum, is described. To analyse the different design criteria, firstly the optical beam propagation and its waist are calculated using the ray transfer matrix analysis (ABCD law) [52], with the relation,

$$\frac{1}{q(z)} = \frac{1}{R(z)} - i\frac{\lambda}{\pi n w^2(z)} \tag{3.7}$$

where $w(z)$ is the radius of the beam size dependent on the z-position, n is the refractive index, $R(z) = z(1 + (z_R/z)^2)$ is the radius of curvature of the beam, with $z_R = n\pi w_0/\lambda$ being the Rayleigh length and w_0 the beam waist. The complex beam parameter, $q(z)$, contains thereby the full information of the Gaussian beam. Gaussian beams remains Gaussian under linear transformation, which allows for the use of the ABCD law. The ABCD law describes how the initial Gaussian beam decribed by q_1, transforms into the final Gaussian beam described by q_2,

$$q_2 = \frac{Aq_1 + B}{Cq_1 + D} \tag{3.8}$$

where the A, B, C, D represents the matrix elements in the final matrix formulation, describing the propagation $1 \rightarrow 2 \rightarrow 3$ by $\mathbf{M} = \mathbf{M_3 M_2 M_1}$. For the optical cavity illustrated in figure 3.5, the matrix formulation becomes,

$$\begin{aligned}
\mathbf{M} &= \begin{bmatrix} A & B \\ C & D \end{bmatrix} \\
&= \mathbf{M_1} \cdot \mathbf{D_1} \cdot \mathbf{Cr_{fl,2}} \cdot \mathbf{D_2} \cdot \mathbf{Cr_{c,2}} \cdot \mathbf{D_3} \cdot \mathbf{M_2} \cdot \mathbf{D_3} \cdot \mathbf{Cr_{c,1}} \cdot \mathbf{D_2} \cdot \mathbf{Cr_{fl,1}} \cdot \mathbf{D_1} \\
&= \begin{bmatrix} 1 & 0 \\ \frac{-2}{\mathrm{RoC_{M1}}} & 1 \end{bmatrix} \cdot \begin{bmatrix} 1 & d_1 \\ 0 & 1 \end{bmatrix} \cdot \begin{bmatrix} 1 & 0 \\ 0 & n \end{bmatrix} \cdot \begin{bmatrix} 1 & d_2 \\ 0 & 1 \end{bmatrix} \cdot \begin{bmatrix} 1 & 0 \\ \frac{1-n}{\mathrm{RoC_{cr}} \cdot n} & 1/n \end{bmatrix} \cdot \cdot \begin{bmatrix} 1 & d_3 \\ 0 & 1 \end{bmatrix} \\
&\quad \cdot \begin{bmatrix} 1 & 0 \\ \frac{-2}{\mathrm{RoC_{M2}}} & 1 \end{bmatrix} \cdot \begin{bmatrix} 1 & d_3 \\ 0 & 1 \end{bmatrix} \cdot \begin{bmatrix} 1 & 0 \\ \frac{n-1}{-\mathrm{RoC_{cr}}} & n \end{bmatrix} \begin{bmatrix} 1 & d_2 \\ 0 & 1 \end{bmatrix} \cdot \begin{bmatrix} 1 & 0 \\ 0 & 1/n \end{bmatrix} \cdot \begin{bmatrix} 1 & d_1 \\ 0 & 1 \end{bmatrix}
\end{aligned} \tag{3.9}$$

with each of the matrices, $\mathbf{M_1} = \begin{bmatrix} 1 & 0 \\ \frac{-2}{\mathrm{RoC_{M1}}} & 1 \end{bmatrix}$, $\mathbf{D_1} = \begin{bmatrix} 1 & d_1 \\ 0 & 1 \end{bmatrix}$, etc. representing each of the ray transfer matrices, describing the propagation or refraction for the given media throughout one round trip in the cavity, as shown in figure 3.5.

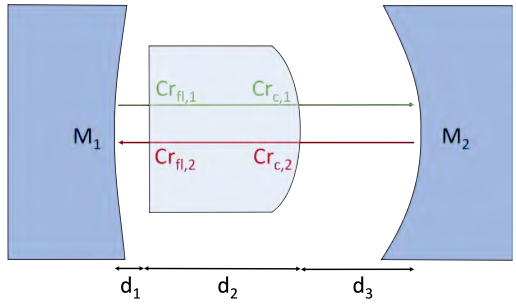

Figure 3.5: Sketch of the optical cavity with the curved crystal inside. The green arrow represents the light propagating in the $+z$ direction, where as the red arrow represents the light propagating in the $-z$ direction, completing one round trip in the cavity.

Mirror, $\mathbf{M_1}$, has a radius of curvature, $\mathrm{RoC_{M1}} = 500$ mm, mirror, $\mathbf{M_2}$, has a radius of curvature, $\mathrm{RoC_{M2}} = 20$ mm, d_1 is the distance between the first mirror and the crystal, d_2 is the distance between the two crystal surfaces, and d_3 is the distance

between the crystal and the last mirror. $\mathbf{Cr_{fl,1}}$ represents the refraction between vacuum and the flat crystal surface with refractive index, n. $\mathbf{Cr_{c,1}}$ represents the refraction between the curved crystal surface with a radius of curvature, $\mathrm{RoC_{cr}} = 200$ mm and vacuum. $\mathbf{Cr_{fl,2}}$, $\mathbf{Cr_{c,2}}$ represents the same refraction, but with the light propagating in opposite direction.

3.4.1 Cavity Stability

Firstly, the stability of the acoustic cavity is considered. The stability criterion is $0 \leq g_1 \cdot g_2 \leq 1$, where the stability parameters, g_1, g_2, are found [30]:

$$g_{1,2} = 1 - \frac{L_{cr}}{\chi \cdot \mathrm{RoC}_{1,2}} \tag{3.10}$$

Here $\mathrm{RoC}_{1,2}$ is the radius of curvature of the two crystal surfaces respectively, with one surface being flat and the other a radius of curvature RoC = 200 mm. $\chi = v_l^2 \frac{v_l^2 - v_t^2}{v_l^2 \cdot v_t^2 - v_t^4 + \gamma_1^4}$ is the anisotropy parameter, where $v_l = \sqrt{c_{33}/\rho}$ is the longitudinal wave velocity, $v_t = \sqrt{c_{44}/\rho}$ is the transverse wave velocity, and $\gamma_1 = \sqrt{(c_{13} + c_{44})\rho}$ is the plane wave velocity. The density is $\rho = 2.650 \cdot 10^3$ kg m^{-3}, and $c_{33} = 106.1 \cdot 10^9$ Nm^{-2}, $c_{44} = 57.8 \cdot 10^9$ Nm^{-2}, and $c_{13} = 12.6 \cdot 10^9$ Nm^{-2} are the relevant elastic constants. This results in $g_1 = 1.0$ and $g_2 = 0.97$ and thus with a product that satisfies the stability criterion.

Subsequently, the stability of the optical cavity is calculated for different cavity lengths and different crystal positions. The stability criterion for the optical cavity is given by:

$$g^2 \leq 1, \quad \text{with} \quad g = \frac{\mathrm{tr}(\mathbf{M})}{2} \tag{3.11}$$

In figure 3.6 the stability parameter, g^2, is shown for cavity lengths between 4 mm and 24 mm and with the crystal positions between 0 mm and 20 mm. The cavity is stable (the red area) for cavity lengths $L_{cav} < 21$ mm, and start to become unstable for cavity lengths $L_{cav} \leq 21$ mm (white and blue area). The dark red area in the lower right corner represents constellations of the cavity, where the crystal is partly or entirely outside of the cavity and is thus not considered for the calculations.

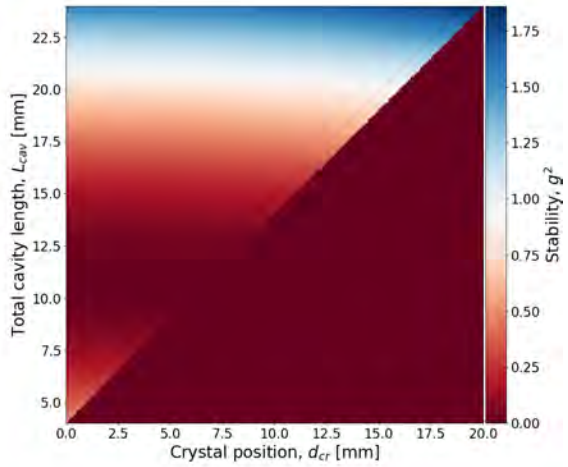

Figure 3.6: Stability of the optical cavity, g^2, as a function of different cavity lengths and crystal positions. The plot shows that the cavity is stable for the constellations of the cavity length between 4 mm - 21 mm and for all possible crystal positions in that range. The cavity becomes unstable for cavity lengths $L_{cav} > 21$ mm. The dark red area in the lower right corner indicates configurations with the crystal partly or entirely outside of the cavity, and is not taken into account in the calculations.

3.4.2 Waist Overlap

To find the best constellation for the cavity, the waist overlap between the optical waist and acoustic waist is calculated. Firstly, the acoustic waist is found [30],

$$w_{0,ac} = \sqrt{\frac{z_{R,ac} \cdot \lambda_{ac}}{\pi \cdot \chi}} \tag{3.12}$$

where the acoustic wavelength is given by $\lambda_{ac} = \lambda_{op}/(2|n|)$, and λ_{op} is the optical wavelength, the acoustic Rayleigh length is, $z_{R,ac} = L_{cr}\sqrt{\frac{1-L_{cr}/(\chi \cdot \mathrm{RoC}_{cr,2})}{L_{cr}/(\chi \cdot \mathrm{RoC}_{cr,2})}}$ and the evolution of the acoustic beam size is found by $w_{ac} = w_{0,ac}\sqrt{1 + (z/z_{R,ac})^2}$.

The optical waist is found as described in section 3.4. The overlap between the

optical and acoustic beams, w_{ov}, is calculated as the ratio between the beam size difference, $w_{ac} - w_{op}$, and the acoustic beam size, w_{ac}, integrated over the length of the crystal, L_{cr}, and then normalised by $1/L_{cr}$:

$$w_{ov} = \frac{1}{L_{cr}} \int_0^{L_{cr}} \left(1 - \frac{|w_{ac}(z) - w_{op}(z)|}{w_{ac}(z)}\right) dz \tag{3.13}$$

This overlap is found for each cavity length, L_{cav}, between 4 mm - 15 mm and for each crystal position, d_{cr}, between 0 mm - 10 mm, plotted in figure 3.7. The plot shows the best overlap (dark red) when the crystal is placed between 2 mm and 4 mm from the first mirror.

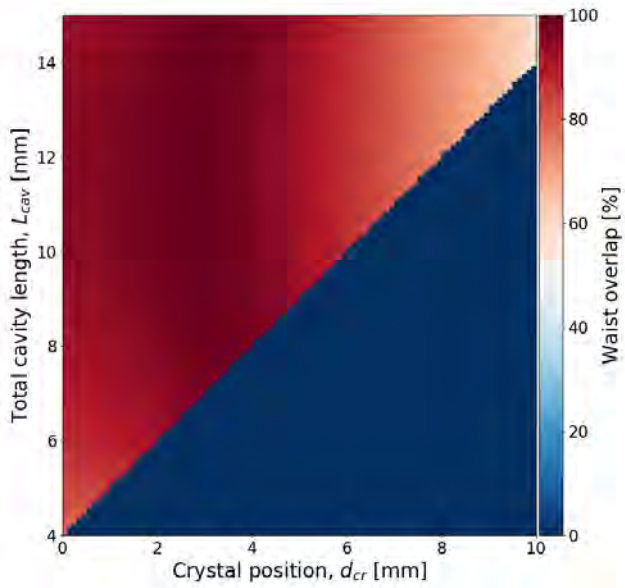

Figure 3.7: Waist overlap (in %) between the optical waist, w_{op}, and acoustic waist, w_{ac}, as a function of the cavity length and the position of the crystal. The waist overlap is largest at the dark red area with a crystal position between 2 mm and 4 mm.

For the final chosen constellation of the cavity, $L_{cav} = 10$ mm and $d_{cr} = 1$ mm (argued for later in this chapter), the acoustic waist is $w_{0,ac} = 75$ μm and the optical waist is $w_{0,op} = 69$ μm and is plotted as a function of z in figure 3.8.

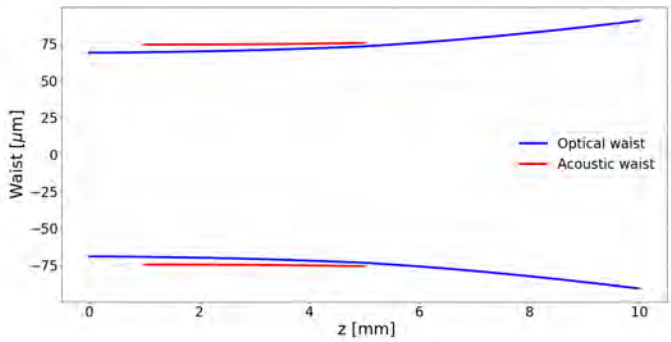

Figure 3.8: Optical waist (blue), w_{op}, and acoustic waist (red), w_{ac}, as a function of z with a cavity length $L_{cav} = 10$ mm and a crystal position at $d_{cr} = 1$ mm.

3.4.3 FSR Spectrum

From the transmission matrix in equation (3.2), the FSR spectrum is found to be asymmetric as previously shown in figure 3.3. An important consideration to take into account for the cavity design is how the FSR spectrum depends on the cavity length and crystal position, such that the configuration supports FSRs that match the Brillouin frequency best. For each pair of adjacent modes, the FSR is calculated and plotted as a function of the wavelength from 1545 nm to 1555 nm, as shown in figure 3.9. Each of the dots represent an FSR and the red dashed line is the expected Brillouin frequency. The plot shows that the FSR oscillates approximately ±2 GHz around the expected Brillouin frequency for this chosen configuration ($L_{cav} = 10$ mm, $d_{cr} = 1$ mm), and that several modes have an FSR close to the expected Brillouin frequency, Ω_m.

When the difference between one FSR and the adjacent FSR, $\Delta\text{FSR} = \text{FSR}_j - \text{FSR}_{j+1}$, is plotted as a function of the FSR, an oval shape appears as shown in figure 3.10. Here every black dot represent the ΔFSR for a given FSR and the dashed red line is the expected Brillouin frequency. The larger the difference between a given FSR and the adjacent FSR, the easier it is to control the Hamiltonian of the system, i.e., suppress either the Stokes or the anti-Stokes process while stimulating the other process.

The pattern appearing for ΔFSR, shown in figure 3.10 depends on the crystal position, d_{cr}, inside the cavity. Simulations of the ΔFSR spectrum and the optical and acoustic waist overlap are made for the different crystal positions, d_{cr}, for

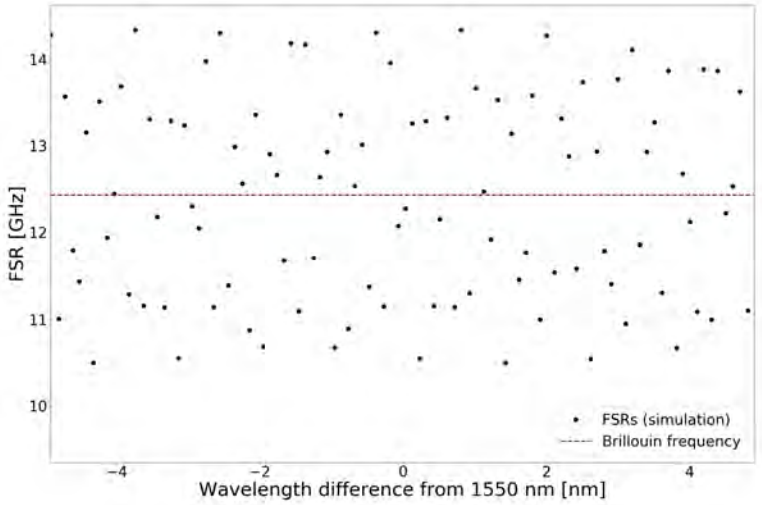

Figure 3.9: Simulation of the FSR as a function of wavelength between 1545 nm and 1555 nm. The black dots represent the FSRs and the red dashed line is the expected Brillouin frequency. The FSR has a spread of about ±2 GHz and distribute evenly around the expected Brillouion frequency. This simulation is made for the constellation with a cavity length, L_{cav} = 10 mm, and a crystal position, d_{cr} = 1 mm.

the optical cavity with the length, L_{cav} = 10 mm. In figure 3.11 and 3.12 are some of the different crystal positions shown; for d_{cr} at 0 mm, 1 mm, 2 mm, 3 mm, 4 mm, and 5 mm. To the left, plots of the difference in FSR, ΔFSR, as a function of the FSR are shown in red. In the upper right corner is a sketch of the cavity with the crystal at different positions. Below, a plot of the optical waist (blue), w_{op}, and the acoustic waist (red), w_{ac}, is shown. It is demonstrated how the spectrum of ΔFSR changes from a shape of a single line at a crystal position, d_{cr} = 0 mm, to broaden to an oval shape for larger and larger distances of the crystal position. When the crystal is in the exact center of the cavity, d_{cr} = 3 mm, a different pattern appears. For the crystal positions, d_{cr} = 4 mm and d_{cr} = 5 mm, the similar oval shapes of the FSR-spectrum appear, similar to the crystal positions, d_{cr} = 2 mm and d_{cr} = 1 mm and thus show a symmetric behaviour around the center.

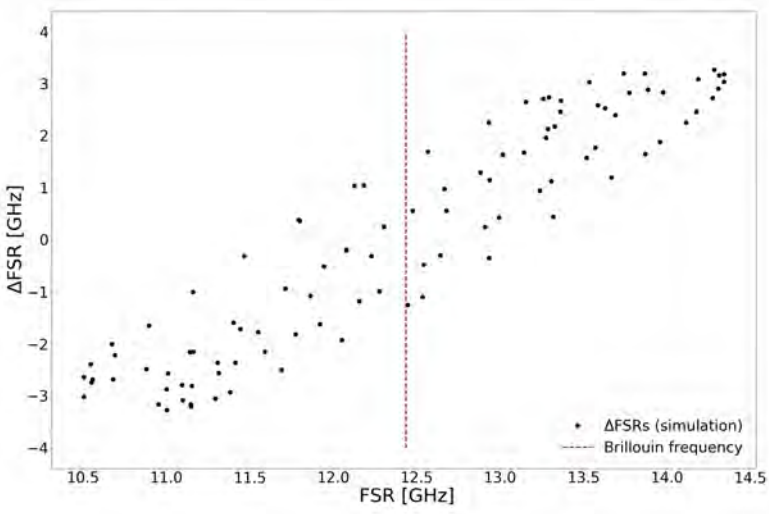

Figure 3.10: Simulation of the difference in FSRs, ΔFSR, as a function of the FSRs for wavelengths between 1545 nm and 1555 nm. The black dots represent the modes, and distribute as an oval shape. The red dashed line is the expected Brillouin frequency. This simulation is made for the constellation with a cavity length, L_{cav} = 10 mm, and a crystal position, d_{cr} = 1 mm.

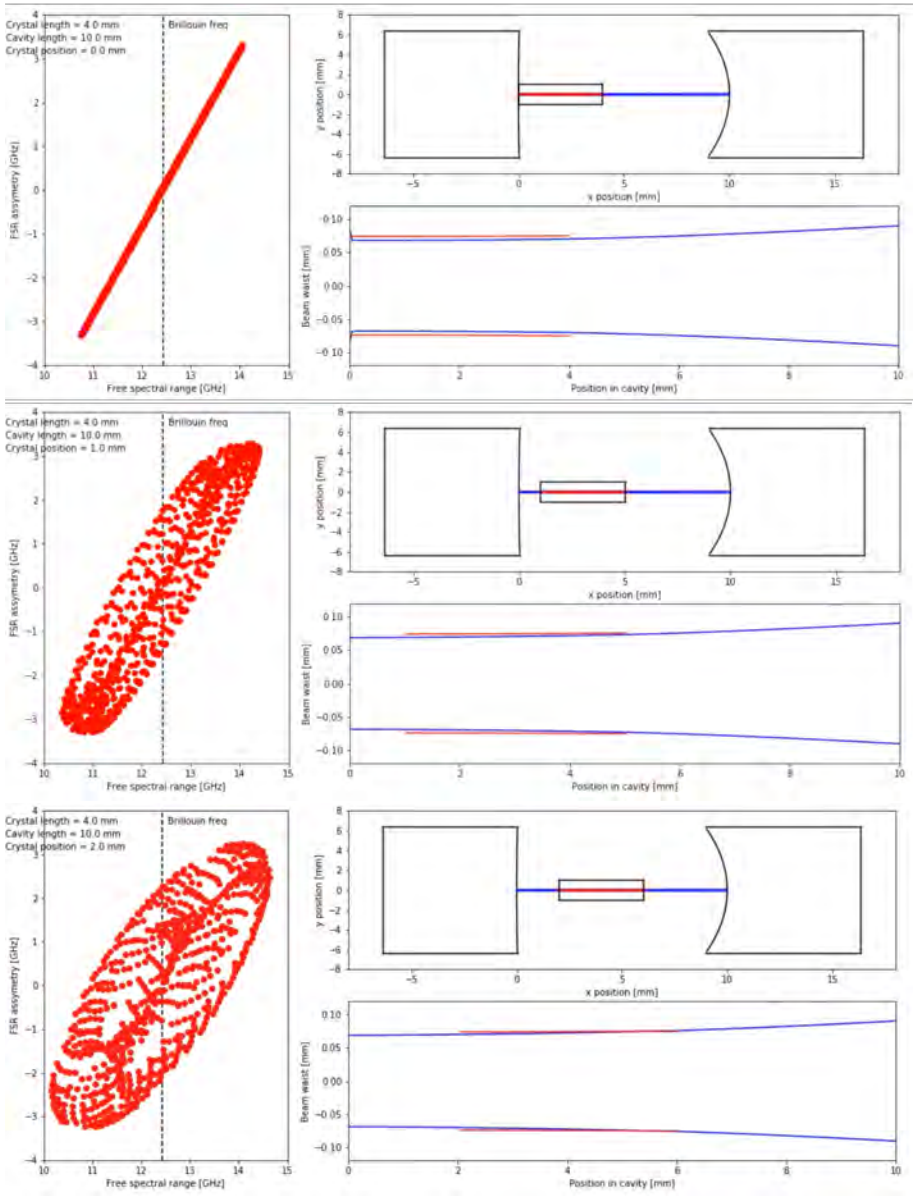

Figure 3.11: Simulation of the ΔFSR spectrum and the optical and acoustic waists, depending on the crystal position in the optical cavity. From the top the crystal is at 0 mm, 1 mm, and 2 mm, distance away from the first mirror. The blue lines represent the optical modes, and the red lines represent the acoustic modes.

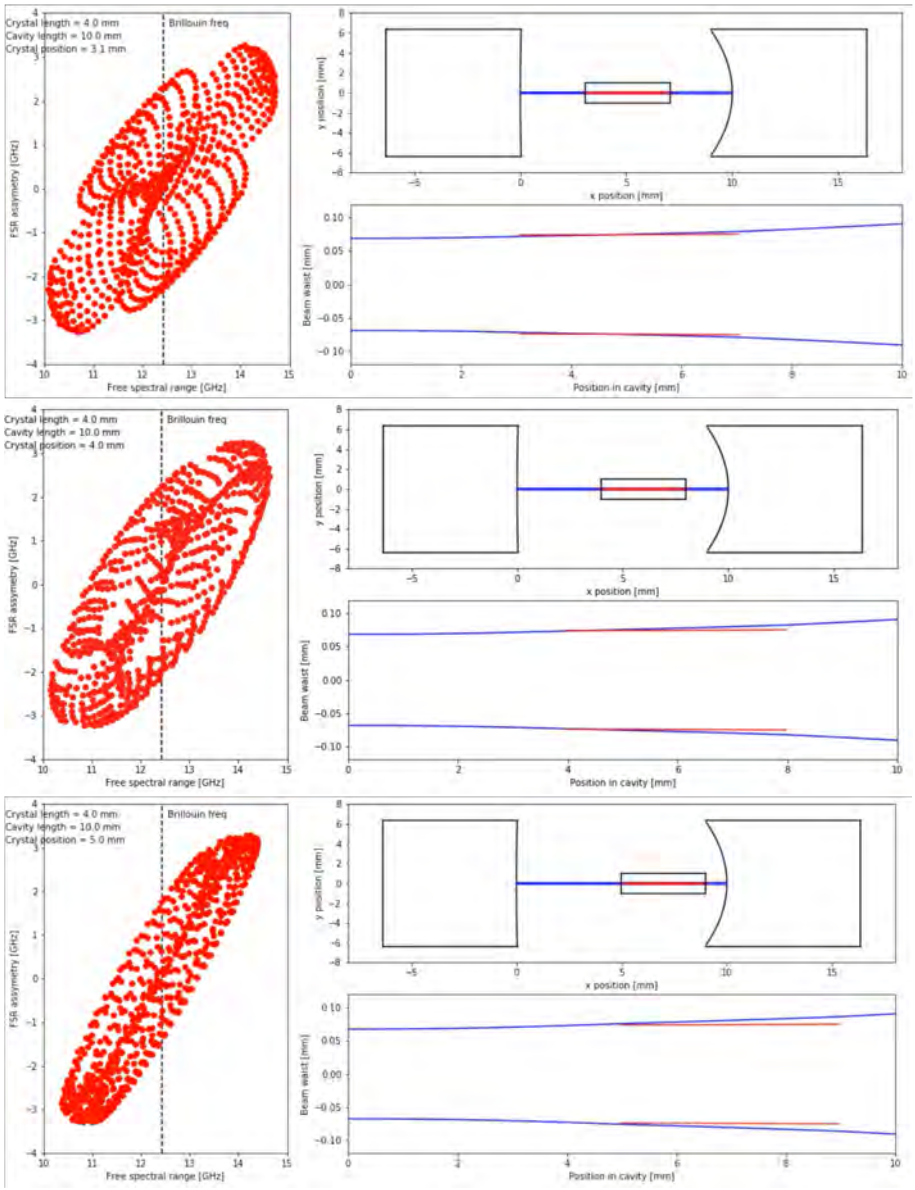

Figure 3.12: Simulation of the ΔFSR spectrum and the optical and acoustic waists, depending on the crystal position in the optical cavity. From the top the crystal is at 3 mm, 4 mm, and 5 mm distance away from the first mirror. The blue lines represent the optical modes, and the red lines represent the acoustic modes.

In order to decide on the chosen configuration (L_{cav} = 10 mm, d_{cr} = 1 mm) used in figure 3.9 and figure 3.10, different aspects of the FSR spectrum were studied. As shown in figure 3.9 the FSR centers around a mean FSR, $\overline{FSR}$, with a spread around δFSR ± 2 GHz. The mean FSR is of course dependent on the length of the cavity. Hence simulations of the varying FSRs are made for cavity lengths between 4 mm to 15 mm, with the crystal at different positions between 0 mm and 10 mm from the first mirror. The interest is to design a cavity where the Brillouin frequency, Ω_m, can be resonant with one of the FSRs. In figure 3.13 a plot is shown for the different cavity lengths and the different crystal positions, where the green area represents the respective ranges where the Brillouin frequency, Ω_m, is within the FSR-range ($\overline{\text{FSR}}$ ± δFSR). The red area represents the ranges for the cavity length and crystal position, where the Brillouin frequency is outside of the FSR-range. So in order to find an FSR that is resonant with the Brillouin frequency, the cavity length must be somewhere in between 9 mm – 11 mm.

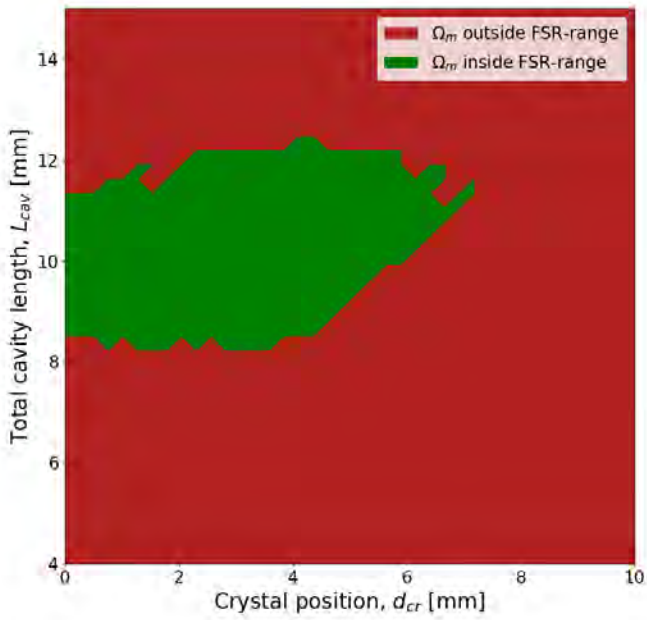

Figure 3.13: Ranges of the cavity lengths and crystal positions where the Brillouin frequency is within the FSR-range (green). If the condition is not met, the ranges are red.

In order to get the best conditions to match the Brillouin frequency, Ω_m, with most possible FSRs, the average FSR, $\overline{\text{FSR}}$, is calculated for the different ranges of the cavity length and crystal position, and is shown in figure 3.14. The average FSR is plotted between 12 GHz and 13 GHz. With a Brillouin frequency on $\Omega_m \sim 12.5$ GHz, (plotted in green), the best match for the average FSR is in the orange area, concluding the best length for the cavity on $L_{cav} = 10$ mm.

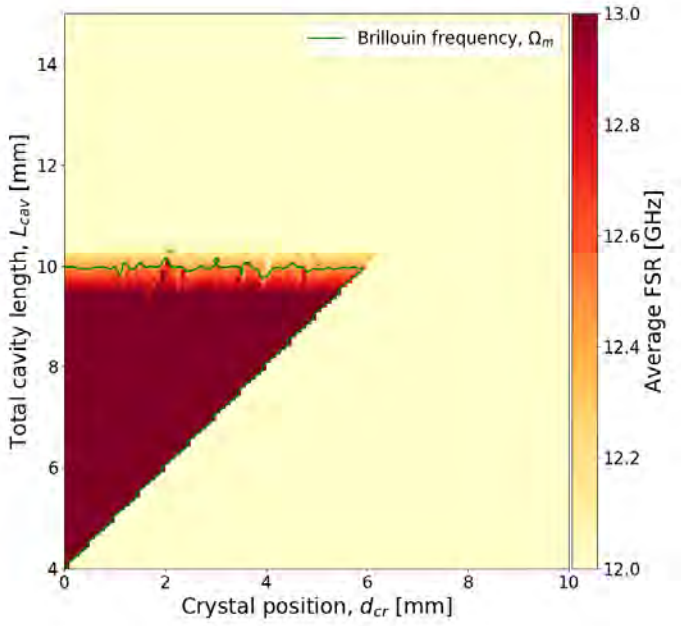

Figure 3.14: The average FSR, $\overline{\text{FSR}}$, plotted as function of the cavity length, L_{cav}, and the crystal position, d_{cr}. The Brillouin frequency on $\Omega_m \sim 12.5$ GHz is plotted in green as a contour plot. The best match for the average FSR and the Brillouin frequency is found at a cavity length on $L_{cav} = 10$ mm.

The difference in FSRs, ΔFSR, describes the amount of asymmetry of the FSR spectrum. The larger the asymmetry, the easier it is to distinguish and suppress a Stokes measurement from an anti-Stokes measurement or vice versa. In figure 3.15 the average difference of the FSR, $\overline{\Delta\text{FSR}}$, is plotted as function of the different cavity lengths and crystal positions. For cavity lengths around 10 mm, the largest asymmetry (largest average difference in FSR, $\overline{\Delta\text{FSR}}$) is found with a crystal position closest to the first mirror or closest to the second mirror

(represented by the white areas). With a crystal position close to the second mirror, the waist overlap is not as good as when the crystal is close to the first mirror (shown in figure 3.7). Furthermore the optical waist is located close to the first cavity mirror. For these reasons the preferred design constellation is chosen to be a cavity length of L_{cav} = 10 mm and a crystal position of d_{cr} = 1 mm.

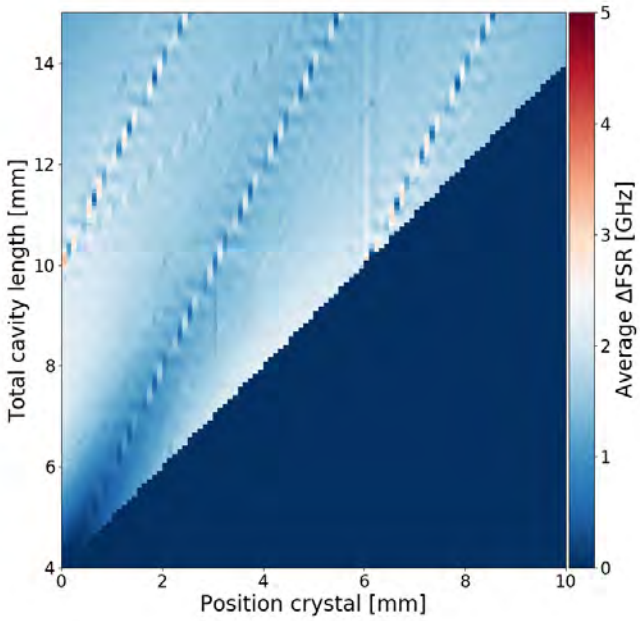

Figure 3.15: The average difference in FSR, $\overline{\Delta\text{FSR}}$, plotted as a function of the cavity length, L_{cav}, and the crystal position, d_{cr}. The largest asymmetry of FSRs appears to be with a crystal position close to one of the mirrors (represented by the white areas), if the cavity length is 10 mm.

3.5 Design of Room Temperature Cavity

The first cavity design presented, is designed for the room temperature experiment. The in depth design of the cavity for milli-Kelvin temperatures is presented in chapter 5. In figure 3.16 a Solidworks model of the room temperature cavity is shown. The total cavity length is L_{cav} = 10 mm and the 4 mm flat-flat-faceted z-cut quartz crystal is placed at d_{cr} = 1 mm from the first mirror. The cavity holder is designed in brass and consists of four main parts: Two end caps with an aperture for the light to enter and leave the cavity, a lid on top (which is not shown on the sketch), and the central part containing the mirrors, the crystal holder with crystal, and spacers. The central part has a v-groove cut out in the center, such that the mirrors fall easily into place and help the mirrors align.

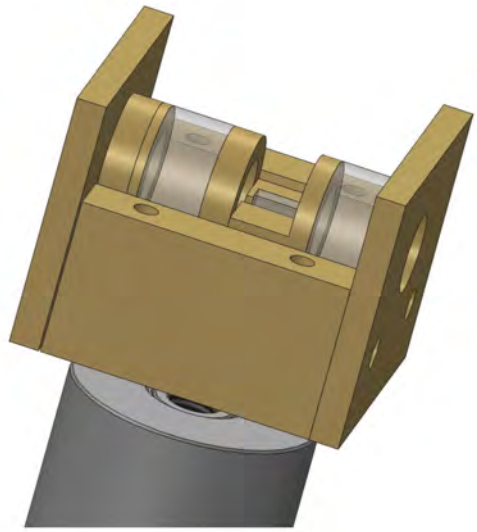

Figure 3.16: A Solidworks model of the room temperature cavity design. The cavity holder is made of brass with apertures on each end-cap, for the light to enter from the right and be transmitted in the other end of the cavity. The mirrors are shown in light transparent grey as well as the rectangular cuboid crystal in the center.

Chapter 4

Coupling between Light and Bulk Acoustic Waves at Room Temperature

In the previous chapter, the physical criteria and general design considerations for the optomechanical cavity were presented. In this chapter, the experimental results on Brillouin lasing and strong coupling are presented for the optomechanical cavity operated at room temperature.

4.1 Experimental Setup

As described in the previous chapter, the optomechanical system consists of a Fabry-Pérot interferometer of two highly reflecting mirrors separated by the distance $L = 1$ cm, with a 4 mm long z-cut quartz crystal placed between them. The cavity (figure 4.1a) is held in a brass holder with a v-groove to let the mirrors self align, shown in figure 4.1b.

In figure 4.2 a simplified schematic of the experimental setup is shown. The system is designed for telecom wavelengths, and the cavity is pumped at

(a)

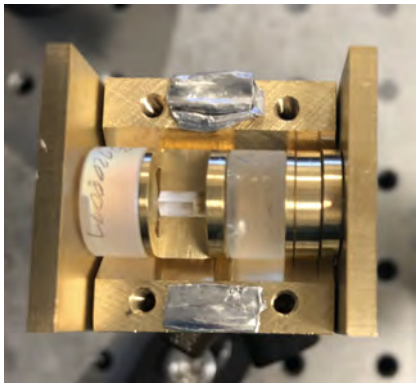

(b)

Figure 4.1: **(a)** The optomechanical cavity in its brass holder, with a peltier and heat sink on top. The cavity holder is held together by nylon screws in order to prevent heat transfer between the brass holder and the lid with the heat sink. **(b)** The brass holder is depicted open and shows the v-groove that supports the mirrors, crystal-holder, and spacers to self align (see also figure 4.4). Indium foil is placed in between the surfaces of the brass holder parts for thermal contact and to soften the clamping.

a wavelength of 1550 nm using a tunable diode laser (Toptica, CTL), with a linewidth < 10 kHz. The first part of the setup is fiber coupled and is represented with blue lines in figure 4.2, while the free space optics is represented with red. The pump is split by a 75/25 fiber beam-splitter, where one part - the local oscillator (LO) is frequency shifted by +80 MHz using an acousto-optic modulator (AOM) (Gooch & Housego, T-M080-0.4C2J-3-F2P). The other part is sent to an electro-optic modulator (EOM) (Thorlabs, LN27S-FC), generating sidebands at variable frequencies around 12.5 GHz. The signal from the cavity is measured in reflection with unbalanced heterodyne detection, using a fast detector (Thorlabs, DX20AF) with 20 GHz bandwidth.

A frequency synthesizer (AnaPico, APSYN420-2) with two output channels, is used to generate frequencies for the EOM and for down conversion using a mixer (Mini-Circuits, ZX05-24MH-S+) after detection of the signal. Down conversion of the measured frequencies ($\sim$ 12 GHz) is necessary in order to acquire the data from a spectrum analyser with frequency range of 9 kHz – 3 GHz. The frequency scans sent to the EOM and for down conversion, respectively, are synchronised such that the difference in frequencies from the two channels stays the same throughout the scans and enable the signal from the cavity to be measured in a

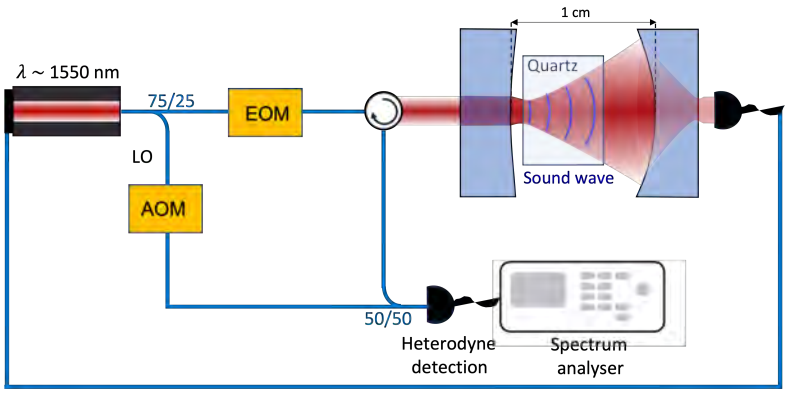

Figure 4.2: Simplified schematic of the experimental setup. The blue lines represent fiber coupled optics, while the red lines represent free space optics. The pump at 1550 nm is split by a 75/25 fiber beam-splitter, where one arm, the local oscillator (LO), is frequency shifted +80 MHz by an AOM, and the other arm is sent through an EOM to generate variable sidebands at frequencies around 12.5 GHz. The pump, now in free space after the circulator, is sent to the optomechanical cavity consisting of a high finesse optical cavity with a 4 mm sized quartz crystal inside. The measured transmission is sent to the laser for the laser lock. The signal is measured in reflection by heterodyne detection, and data is acquired on the spectrum analyser and subsequently sent to the computer.

zero-span measurement with a spectrum analyser (Keysight Technologies, CXA N9000A), where the measurements are acquired using a resolution bandwidth of 0.5 kHz. To acquire high enough powers for the experiment, a laser amplifier (NKT, Koheras BOOSTIK LC) is used. The entire experiment is controlled by custom made software running on Qudi [54]. In figure 4.3 the experiment is depicted from above the optical table.

For the cavity, two high reflecting mirrors are used, with different radia of curvature (RoC). The in-coupling mirror (LayerTec) has a RoC = 500 mm and a transmission T = 500 ppm. The end mirror has custom made coating (LaserOptik) and has a RoC = 20 mm and a transmission T = 40 ppm. The 4 mm long z-cut flat-faceted quartz crystal (Shalom EO) is placed 1 mm from the first mirror. The transmission from the cavity is measured and fed back to the laser, to lock the cavity. The laser uses a build-in locking system that creates the error signal by modulating and de-modulating the frequency.

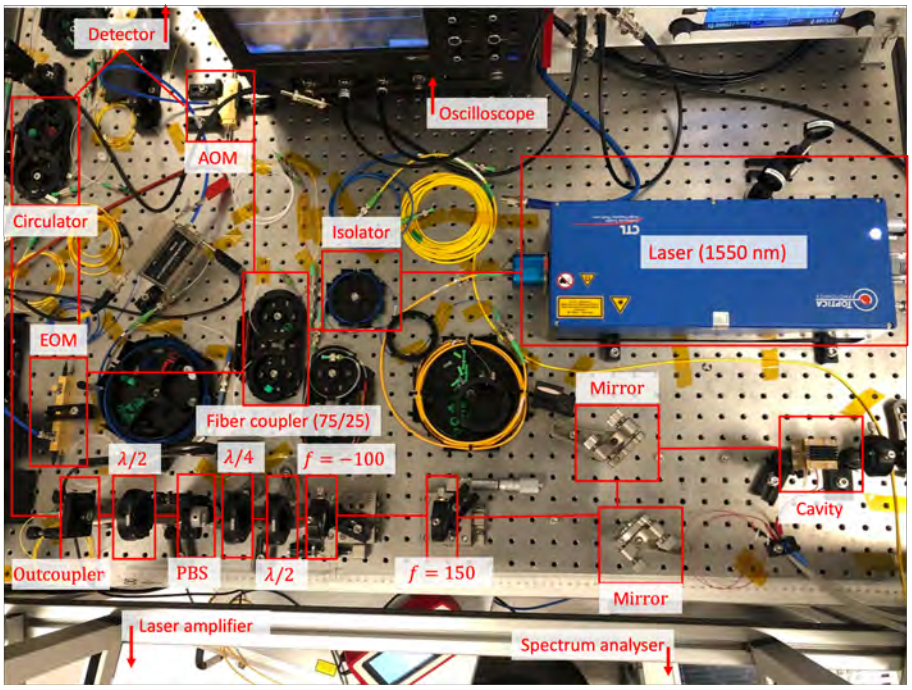

Figure 4.3: Experimental setup depicted from above the optical table. The red lines between each device represents the path of the light. The fiber-coupled laser pump (at 1550 nm) is first send through an isolator and then split by the 75/25 fiber beam-splitter, where one part of the pump, the local oscillator is frequency shifted +80 MHz by the AOM, and the other part is sent to the EOM, where variable sidebands are generated around 12.5 GHz. Before coupling to free space, the pump is sent through a circulator. In free space, the pump is sent through a half-wave plate ($\lambda/2$), a polarising beam-splitter (PBS), a quarter-wave plate ($\lambda/4$), and a half-wave plate ($\lambda/2$) before sent to the two mode-matching lenses with focal length of $f = -100$ mm and $f = 150$ mm, respectively. The two steering mirrors are used to guide the beam to the cavity, where the transmission is sent to the laser for the laser lock. The reflection is via the circulator sent to a 50/50 fiber beam-splitter, that combines the signal and local oscillator for heterodyne detection.

4.1.1 Modifications

Several modifications were implemented to improve the initial experimental design. These modifications were crucial for accomplishing the experimental results shown later in this chapter. Firstly, the crystal holder was modified for better alignment of the crystal. Instead of placing the crystal on a flat holder, where it easily got misaligned by small vibrations, it now falls into a v-groove and self align, as shown in figure 4.4. In order to get better thermal contact, thermal paste was applied on the surfaces of contact.

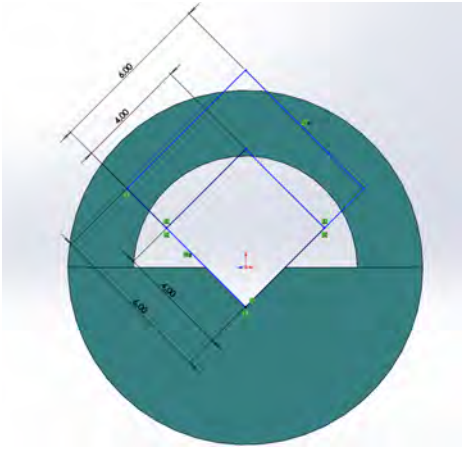

Figure 4.4: Solidworks sketch of the revised crystal holder shown as a cut-through.

In order to tune the modes in and out of the Brillouin zone, an adapter for the cavity was designed to add a peltier and a heat sink, shown in figure 4.1a to the left. To control the temperature of the peltier, a temperature controller (Thorlabs, TC200) with 0.1°C resolution was first used. As the resolution was not high enough to have complete control over the modes, the setup was upgraded with a new temperature controller (Thorlabs, TED4015) with a resolution of 0.001°C to gain better control of the detuning.

Furthermore the measurement scheme was upgraded in a way that decreased the measurement time from 10-20 minutes to ~ 1 minute after replacing a noisy (and not tunable) VCO (Analog Devices, HMC1166) with a two-channel low noise tunable frequency synthesizer (AnaPico, APSYN420-2). This allowed to synchronise the frequency sweeps send to the EOM and the frequency sweeps send to the mixer for down conversion, making it possible to perform a zero-span measurement on the spectrum analyser. This improvement allowed to extract the data of an entire frequency sweep in one go, whereas the earlier stage of the

experiment, one data-point for each frequency step in the frequency sweep was extracted one at a time and subsequently all data-points were recombined for one frequency sweep in Qudi (on the computer).

4.1.2 Characterizations

As described in the previous chapter, the reflection from the surfaces of the crystal contribute to a coupled cavity system. The coupled cavities manifest an asymmetric free spectral range (FSR). When scanning the wavelength from 1545 nm to 1555 nm, the asymmetric FSR-spectrum is apparent, see figure 4.5. It emerges that both the FSR, linewidth, and intensity are different from mode to mode (a zoom-in of three modes is shown in figure 4.7).

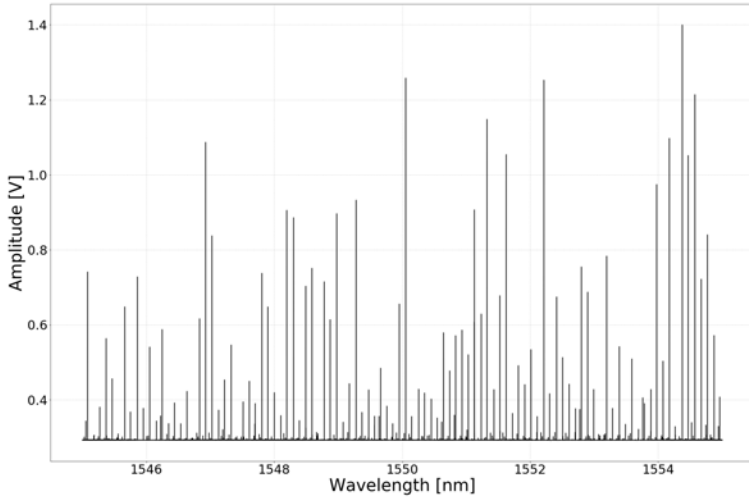

Figure 4.5: Wavelength scan of the transmission from 1545 nm to 1555 nm. The asymmetry of the FSR spectrum is displayed as well of the different intensities and linewidths of each mode.

For each mode, the FSR is found and plotted against the wavelength, seen in figure 4.6a and matches with the simulations presented in figure 3.9 in chapter 3. The red dashed line is the expected Brillouin frequency for quartz at room temperature and the modes with FSR closest to the Brillouin frequency are chosen for measurement.

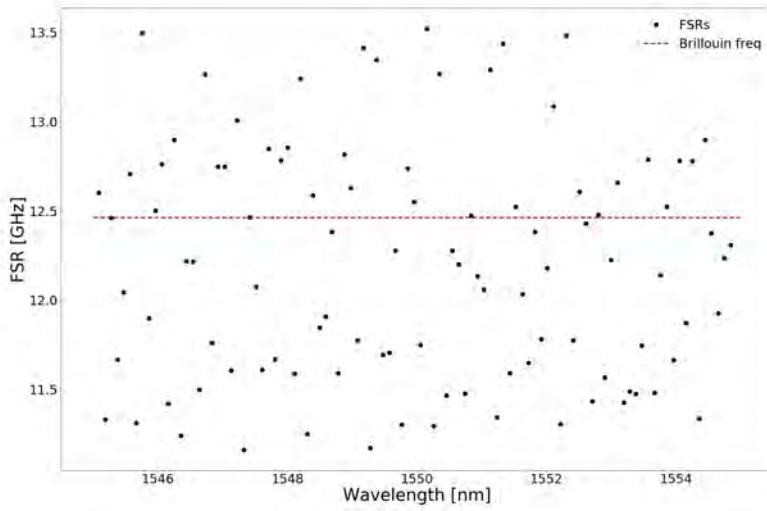

(a)

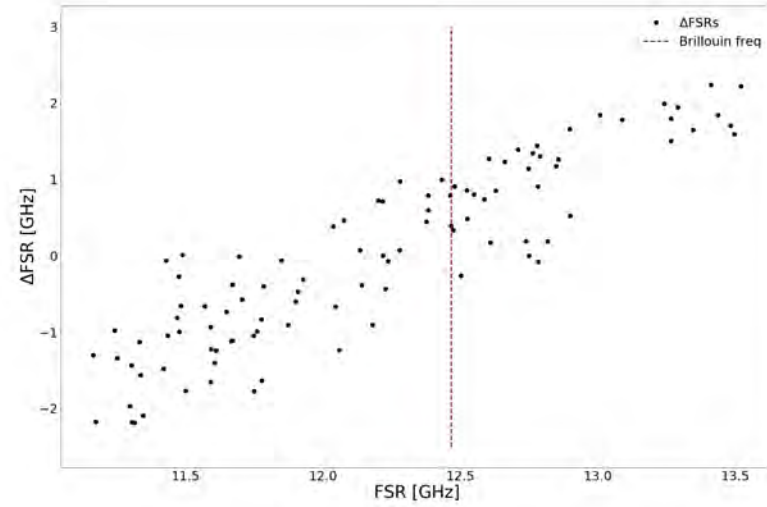

(b)

Figure 4.6: **(a)** FSR plotted against the wavelength, where each dot represents an FSR and the dashed red line is the expected Brillouin frequency for quartz at room temperature. **(b)** Difference between the FSR and the adjacent one, ΔFSR, is plotted as a function of the FSRs. The red dashed line is the expected Brillouin frequency in quartz.

The difference from one FSR to the adjacent FSR, ΔFSR, is calculated and plotted as a function of the different FSRs, seen in figure 4.6b. The expected Brillouin frequency is plotted with a dashed red line. Again, the measurement shows comparability with the simulations of the system presented in figure 3.10 in chapter 3.

Zooming in on the chosen mode around 1550.9 nm, with an FSR close to the Brillouin frequency, three fundamental modes are shown with different FSRs, in figure 4.7.[1]

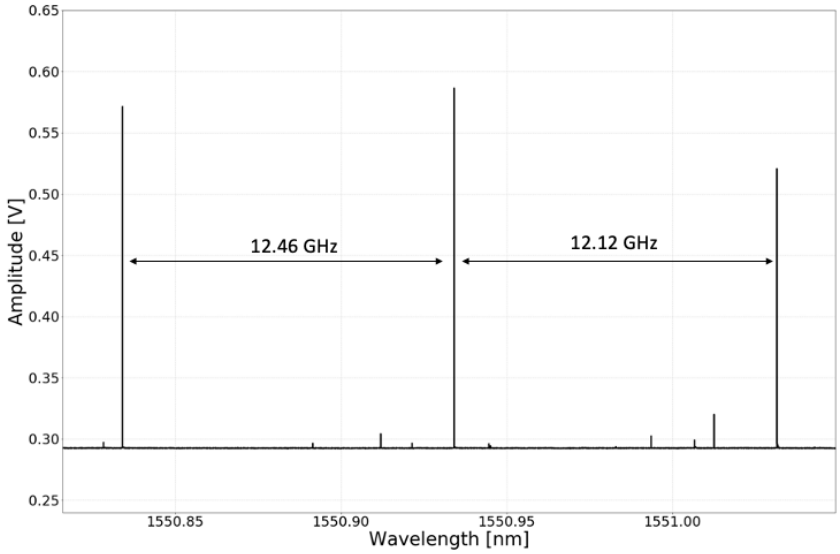

Figure 4.7: A zoom-in on wavelengths around 1550.9 nm of the wavelength scan in figure 4.5. The two optical modes chosen for measurements have an FRS of 12.46 GHz, where one neighbouring mode is shown to display the asymmetry of the mode spacing.

Characterization of the chosen optical mode was done by measuring in reflection. The mode was detuned away from the Brillouin zone, by tuning the temperature, such that only the optical response was measured. The data was fitted to a Lorentzian fit, shown in figure 4.8, where the linewidth, κ (full width half maximum, FWHM), and its standard deviation, σ_κ, was measured to be

[1] The modes used for characterisation, are the ones used for the strong coupling measurements. The Brillouin lasing measurements were carried out for another mode at 1552.27 nm.

$$\kappa = (1.00 \pm 0.03)\ \text{MHz} \tag{4.1}$$

The standard deviation, $\sigma_\kappa = 0.03$ MHz, was obtained from the diagonal elements of the covariance matrix from the fit, $\sigma_\kappa^2 = V_{ii} = \text{cov}(x_{(i)}, x_{(i)})$, where $x_{(i)}$ is the i^{th} entry in the covariance matrix [55]. For this specific mode of interest, with an FSR of 12.46 GHz and an optical linewidth of $\kappa = 1$ MHz, the finesse becomes $\mathcal{F} = \text{FSR}/\kappa \simeq 12.5 \cdot 10^3$.

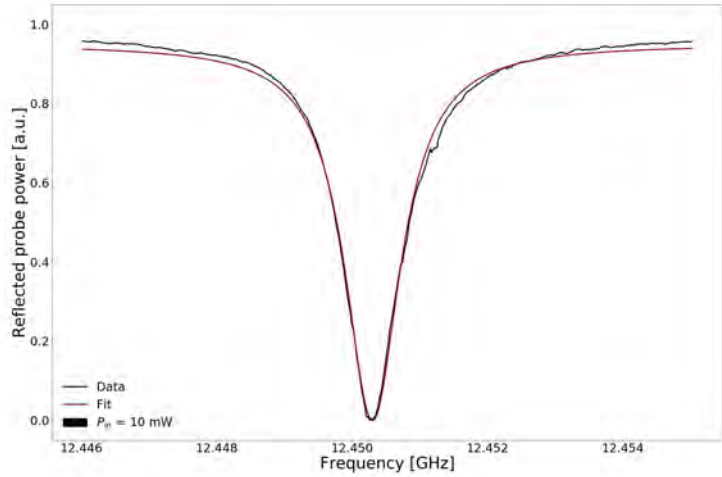

Figure 4.8: Measurement of the optical mode fitted to a Lorentzian with a linewidth (FWHM), $\kappa = (1.00 \pm 0.03)$ MHz.

4.2 Brillouin Lasing

In this part of the experiment, the Stokes process is measured. This is a heating process, described by the two-mode-squeezing Hamiltonian, and creates phonons at the Brillouin frequency. As shown in the schematic in figure 4.9, the pump is locked to the optical mode, ω_j, at a wavelength around 1550 nm, represented with an yellow arrow. The adjacent mode at the Stokes side, ω_{j-1}, is tuned into resonance with the Brillouin frequency, by changing the temperature of the optomechanical cavity. When the FSR is equal to the Brillouin frequency, photons will resonantly scatter (represented with yellow dashed line) from the laser pump at ω_j into the mode one FSR away at the lower frequency, ω_{j-1}, and create phonons at the Brillouin frequency, Ω_m. For these measurements, no sidebands were created using the EOM to probe the cavity mode at ω_{j-1}.

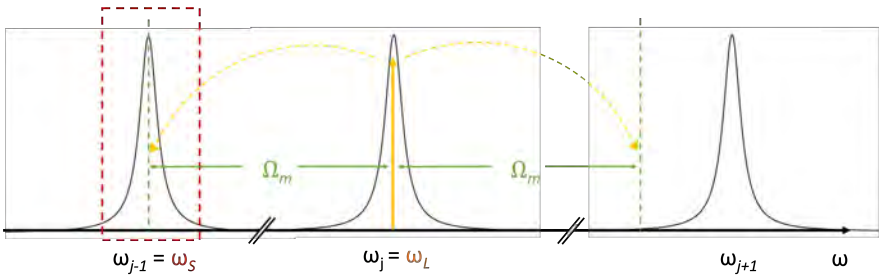

Figure 4.9: Schematics of Brillouin lasing measurement. Three modes are shown with two different FSRs, where only the FSR between mode ω_j and ω_{j-1} is resonant with the Brillouin frequency, represented with the green lines. The yellow arrow represents the laser pump and the yellow dashed lines indicate the scattered photons at the Brillouin frequency. The red dashed line represents the measurement window.

At room temperature the acoustic dissipation rate in crystalline quartz ($\Gamma \simeq$ 10 MHz) is much larger compared to the optical dissipation rate ($\kappa \simeq 1$ MHz) of the cavity. When this hierarchy for the dissipation rates, $\Gamma > \kappa$, is satisfied, it enables exponential amplification of the optical field above lasing threshold. Nonlinear effects increase the acoustic oscillations until they saturate, reaching a steady-state [39]. Brillouin lasing then occurs when the gain from stimulated Brillouin scattering exceeds the round-trip losses. When the pump power becomes greater than the threshold power, the Stokes field builds up from the spontaneous emission to a coherent Stokes emission at the frequency $\omega_S = \omega_l - \Omega_m$ [56].

In figure 4.10 a single measurement of stimulated Brillouin lasing is shown,

with a measured Brillouin frequency of $\Omega_m \simeq 12.443$ GHz. The measurements were carried out for a cavity mode at $\simeq 1552.27$ nm, which gives an estimated Brillouin frequency of $\Omega_m \simeq 12.45$ GHz from equation (3.6). The Brillioun lasing is measured for different input powers shown in figure 4.11. It displays how the system achieves the oscillation threshold power for input powers above 15 mW, and a lasing effect is observed. The Brillouin lasing beam is produced with a signal-to-noise ratio of 40 dB with respect to the shot-noise level.

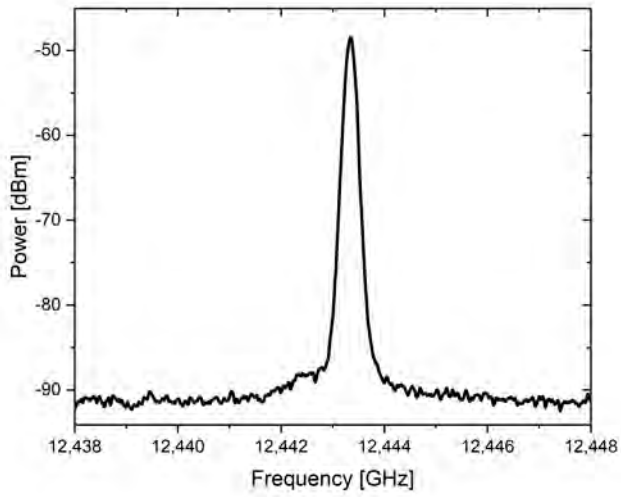

Figure 4.10: Stimulated Brillouin lasing at a Brillouin frequency ~ 12.443 GHz resonant with cavity mode at $\simeq 1552.27$ nm.

The input power of $P_{in} = 15$ mW corresponds approximately to an intra-cavity power of $P_{cav} \simeq 119$ W, given at zero detuning by $P_{cav} = 2\eta\frac{\mathcal{F}}{\pi}P_{in}$ [57]. Where $\mathcal{F}$ is the finesse and the coupling parameter $\eta = \kappa_{ex}/\kappa$. κ is the measured optical linewidth and is a sum of two separate contributions: $\kappa = \kappa_{ex} + \kappa_0$. κ_{ex} is the loss rate related to the input coupling and κ_0 is the remaining loss rate [50]. It is assumed that the main loss is from the in-coupling mirror such that $\kappa_{ex} \simeq \kappa$.

The observed Brillouin lasing is complementary to that of phonon lasing, produced by opto-mechanical self oscillation [58], [59]. However, a Brillouin laser is to be distinguished from phonon lasing, that involves stimulated emission of phonons, where a Brillouin laser involves stimulated emission of Stokes photons.

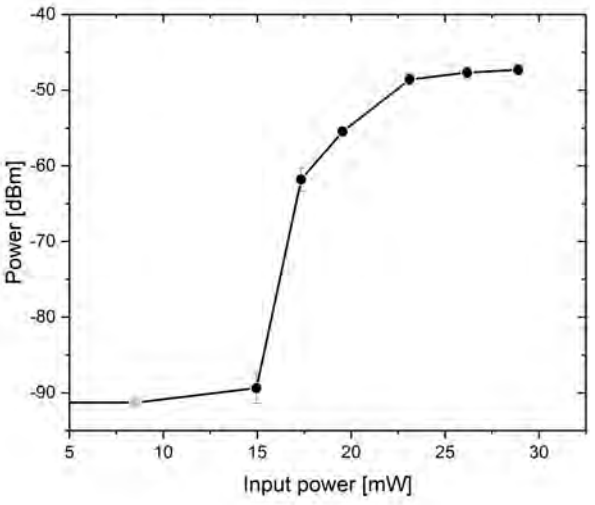

Figure 4.11: Brillouin lasing power as a function of input power. The system achieves oscillation threshold power for input powers above 15 mW corresponding to an intra-cavity power of approximately 740 mW, and shows lasing effects.

4.3 Strong Coupling between Light and Bulk Acoustic Waves

4.3.1 Introduction

Strong coupling between an optical mode and a mechanical (or acoustic) mode is obtained when the coupling, G, exceeds the common mode dissipation rate of the optics and mechanics, which will result in a hybridisation of the two modes. When an optomechanical system is operating in the strong coupling regime, it allows for coherent state transfers, between the optics and mechanics. It is of high interest to obtain strong coupling for an optomechanical system in its quantum ground state, as it will allow for quantum coherent state transfer, and has yet to be achieved. Obtaining quantum coherent state transfer is essential for the development of hybrid quantum technologies, such as quantum memories and quantum transducers, but will also open the door to interrogate fundamental physics, e.g., quantum phenomena in macroscopic objects.

To date only a few cavity optomechanical systems have demonstrated strong coupling, due to different technical challenges related to obtaining a low loss system supporting high coupling rates [51], [37], [35]. Strong coupling has been demonstrated in a Brillouin based macroscopic system with whispering gallery modes in a fused-silica microresonator at room temperature [35]. The high frequency phonons (11 GHz) of the system is advantageous in order to cool the acoustics to the ground state in a dilution fridge, but it is difficult to obtain very low dissipation rates in cryogenic temperatures, because of the amorphous structure in glass [60]. Recently, strong coupling was achieved in a similar system with a high frequency bulk crystalline resonator in a optical cavity at cryogenic temperatures of approximately 10 K [32].

In this section, strong coupling between high frequency bulk acoustic waves and light at telecom wavelength is demonstrated for the optomechanical cavity, with independent control over coupling rate and detuning.

4.3.2 Measurement scheme

For the strong coupling measurements, the anti-Stokes process is probed, which is a cooling process and described by the beam-splitter Hamiltonian. In figure 4.12 a schematic of the measurement is shown. Three fundamental optical modes are shown with asymmetric mode spacing. The laser is locked to the central cavity mode, $\omega_l = \omega_j$, indicated with the yellow arrow. From the pump, photons scatter to each side at the Brillouin frequency, Ω_m, represented with the dashed green lines, where only the anti-Stokes process is resonant. The adjacent mode, one FSR away at higher frequencies, ω_{j+1}, is tuned into resonance with the Brillouin frequency by changing the temperature of the system, such that the measurements are carried out at zero-detuning, $\Delta = \Omega_m + \omega_l - \omega_{j+1} = 0$. To probe this process, two sidebands (represented by the red and blue arrows) are created symmetrically around the pump using an EOM. These sidebands of frequencies around ~ 12.5 GHz are tuned while their reflection is monitored which allows to observe the behaviour of the optical response of the system and from that analyse its optomechanical response. The beating of the sidebands with the local oscillator (LO) (dashed grey line) allow to distinguish the measurement of the red-detuned and blue-detuned sideband, respectively. The detuning of the frequency sweep of the blue-detuned probe, ω_p, in respect to the Brillouin frequency, is denoted by $\delta = \Omega - \Omega_m$, where $\Omega = \omega_p - \omega_l$ is the frequency difference between the laser pump and the probe.

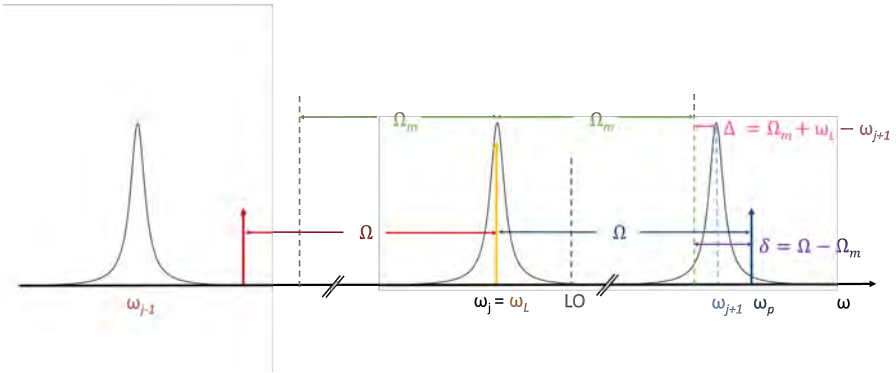

Figure 4.12: Schematics of a strong coupling measurement. Three cavity modes are shown, where the laser is locked to the central mode (represented with the yellow arrow) at $\omega_j = \omega_l$ and the local oscillator (LO) is frequency shifted by +80 MHz (dashed grey line). The red and blue arrows represent the two sweeping sidebands created at the Stokes and anti-Stokes side (ω_p), respectively. The asymmetry of the mode spacing permit to probe only the anti-Stokes process. The green lines represent the Brillouin frequency, Ω_m, and δ (in purple) is the detuning between the probe (sideband) and the Brillouin response. Δ (in pink) is the detuning between the cavity mode ω_{j+1} and the Brillouin response.

4.3.3 Data Processing

For every measurement of the signal, a background measurement is taken, which accounts for the optical response of the setup except for the optomechanical cavity. A background measurement is taken without locking or scanning the cavity. To reduce the random noise, the data is smoothed by a discrete convolution operation, $(f * g)_n = \sum_{m=-\infty}^{\infty} f_m g_{n-m}$ [61]. The convolution is defined as the integral of the product of the two functions, f and g, here corresponding to the measured power at a given frequency, m, where one is shifted in frequency, $m - n$. In practise it becomes a rolling average of the measured data. In figure 4.13a a background measurement before (red) and after (black) the convolution (with a kernel size of 200) of the data is shown.

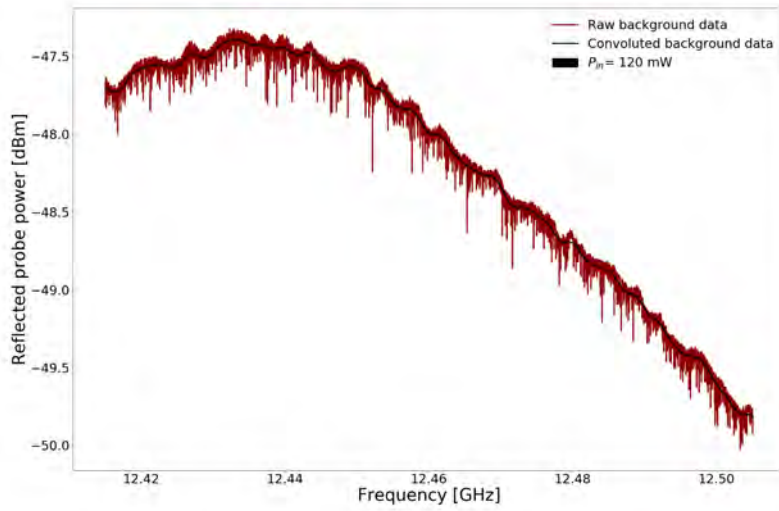

(a)

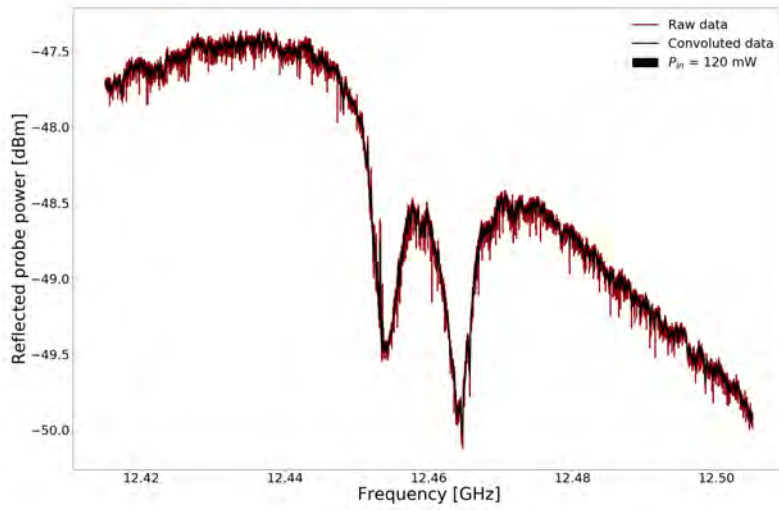

(b)

Figure 4.13: **(a)** Background measurement at an input power of 120 mW. Both the raw background (red) data and smoothed background data (black) is shown. **(b)** Measurement of the signal at an input power of 120 mW. Both the raw data (red) and smoothed data (black) is shown.

The same convolution operation is performed on the signal, but with a kernel size of 10, which is 20 times less than the kernel size of the convolution applied to the background measurements. This is done in order to keep the data of the signal as close to the raw data as possible, but still average out significant noise peaks. The raw data is shown (red) against the convoluted data (black) in figure 4.13b. Lastly the background is subtracted from the signal and then normalised to unity, shown in figure 4.14.

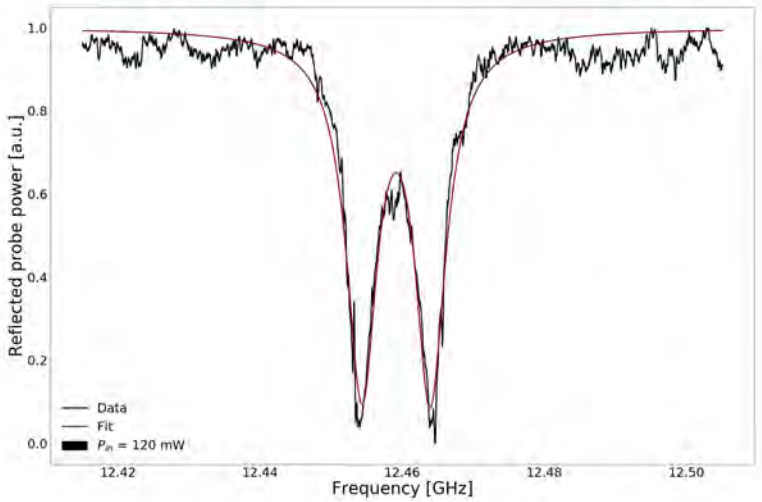

Figure 4.14: Measurement of the signal at an input power of 120 mW. The data is shown after background subtraction and convolution of the background and data. The fit to equation (4.2) is shown in red.

The data of the measured reflected signal is subsequently fitted to the power dependence model for OMIT-measurements derived in section 2.5:

$$P_R = 1 - A \cdot \left| \frac{\kappa_{ex}}{i(\delta + \Delta) - \kappa/2 + \frac{G^2}{i\delta - \Gamma/2}} \right|^2 \tag{4.2}$$

Where A is a scaling parameter and $\kappa = \kappa_{ex} + \kappa_0$ is the optical linewidth. κ_{ex} is the loss rate related to the input coupling and κ_0 is the remaining loss rate. Again, it is assumed that the main loss is from the in-coupling mirror and that $\kappa_{ex} \simeq \kappa$. $\Delta = \Omega_m + \omega_l - \omega_{j+1}$ is the detuning between the cavity

mode at ω_{j+1} and the Brillouin response. For these measurements, the data is acquired at zero detuning, $\Delta = 0$, such that the peak splitting is symmetric. $\delta = \Omega - \Omega_m = \omega_p - \omega_l - \Omega_m$ is detuning of the frequency sweep of the pump at ω_p in respect to the Brillouin response. G is the coupling strength and Γ the acoustic linewidth. For the specific fit shown in figure 4.14 the fitting parameters are presented in table 4.1.

Parameter	Value	Uncertainty	Unit
A	53	4	
κ	1.00	0.03	MHz
Γ	9.4	0.7	MHz
G	5	1	MHz
Ω_m	12.459	0.002	GHz

Table 4.1: Fitting parameters for fit shown in figure 4.14. Data was acquired at a power in front of the cavity at $P_{in} = 120$ mW.

16 measurements at different powers were taken at zero detuning, $\Delta = 0$, between the FSR and the Brillouin frequency, i.e., FSR $= \omega_{j+1} - \omega_j = \Omega_m$. Six of these measurements are presented in figure 4.15, where the power in front of the cavity was measured to be 31 mW, 100 mW, 120 mW, 140 mW, 191 mW, and 223 mW, respectively.

4.3.4 Results

For each of the different power measurements, the data was fitted to the model described in equation (4.2). From each fit the values and uncertainties for the Brillouin frequency, $\Omega_{m,i} \pm \sigma_{\Omega_{m,i}}$, coupling strength, $G_i \pm \sigma_{G,i}$, and the acoustic linewidth $\Gamma_i \pm \sigma_{\Gamma,i}$ were extracted. The standard deviation, $\sigma_{\Gamma,i}$, was obtained from the the diagonal elements of the covariance matrix, $\sigma^2_{\Gamma,i} = V_{ii} = \mathrm{cov}(x_{(i)}, x_{(i)})$ [55], extracted from each fit. The mean value for the acoustic linewidth, $\bar{\Gamma} = \frac{1}{N}\sum_{i=1}^{N} \Gamma_i$, and the accumulated error, $\sigma_\Gamma = \sqrt{\frac{1}{N}\sum_{i=1}^{N} \sigma^2_{\Gamma,i}}$, was calculated to be [62]:

$$\frac{\Gamma}{2\pi} = (10.6 \pm 0.9)\ \mathrm{MHz} \tag{4.3}$$

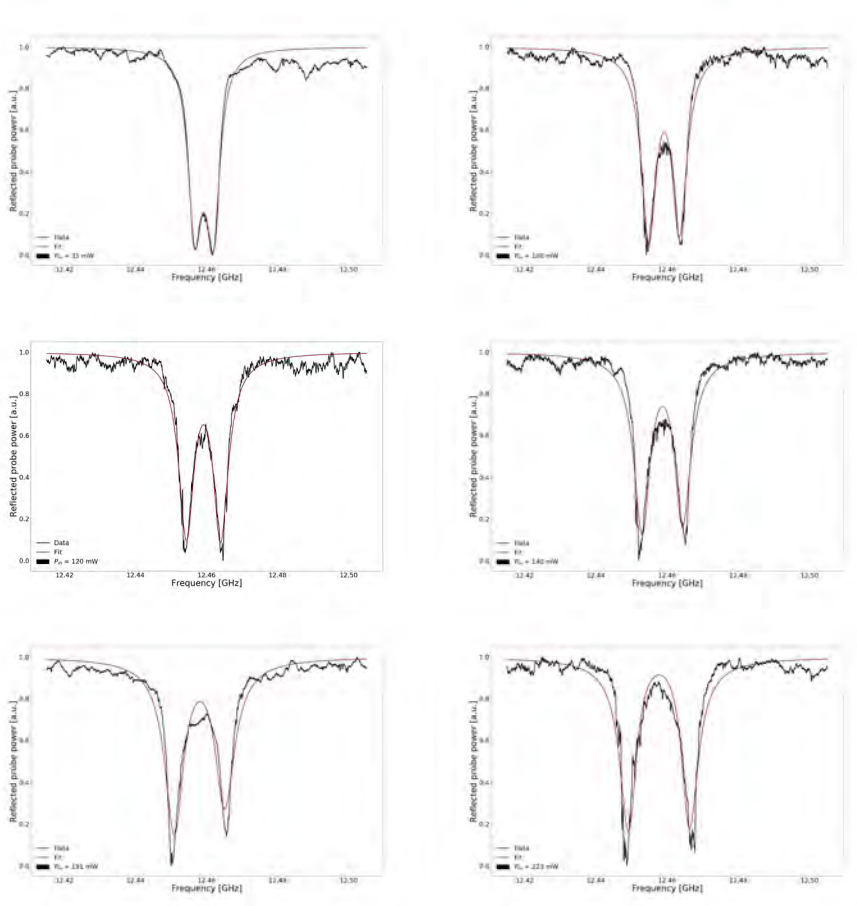

Figure 4.15: Measurements at different powers. From the upper left corner the input power is: 31 mW, 100 mW, 120 mW, 140 mW, 191 mW, 223 mW. The processed data is shown in black, where the fits are shown in red. For each measurement the Brillouin frequency, Ω_m, the acoustic linewidth, Γ, and the coupling strength, G, were extracted from the fit.

The mean and accumulated error for the Brillouin frequency, $\Omega_{m,i} \pm \sigma_{\Omega_{m,i}}$, was found to be:

$$\frac{\Omega_m}{2\pi} = (12.459 \pm 0.003)\ \text{GHz} \tag{4.4}$$

The coupling strength, G, depends on the product of the single photon coupling strength, g_0, and the square root of the average intra-cavity photons, $\bar{N}_{cav}$:

$$G = g_0 \sqrt{\bar{N}_{cav}} \tag{4.5}$$

For each of the different measured input powers, P_{in}, the average intra-cavity photon number, $\bar{N}_{cav}$, was calculated [39]:

$$\bar{N}_{cav} = |\langle a \rangle|^2 = \frac{\kappa_{ex}}{\Delta_l^2 + (\kappa/2)^2} \frac{P_{in}}{\hbar \omega_l} \tag{4.6}$$

Here, $\Delta_l = \omega_l - \omega_j$ is the laser detuning (not to be confused with Δ). Since the laser is locked to the mode at ω_j, $\Delta_l = 0$. Each value of the coupling strength and uncertainty, $G_i \pm \sigma_{G,i}$, extracted from the fits shown in 4.15, are plotted against the input power, P_{in}, on the ordinary x-axis and the average intra-cavity photon number, $\bar{N}_{cav}$, on the secondary x-axis, shown in figure 4.16. The fit (shown in red) of the measured coupling strengths, G, follows the square-root dependence of the average intra-cavity photon number, $\bar{N}_{cav}$, as expected from equation (4.5). The single photon coupling, g_0, and its uncertainty were estimated from the fit:

$$\frac{g_0}{2\pi} \simeq (1.2 \pm 0.2)\ \text{Hz} \tag{4.7}$$

which is comparable with the theoretical (orders of magnitude) estimation from equation (2.23),

$$\frac{g_0^{(th)}}{2\pi} \approx \frac{\omega_j^2 n^3 p_{13}}{2c} \sqrt{\frac{\hbar}{\Omega_m \rho A L_{cr}}} \left(\frac{L_{cr}}{L_{cav}}\right) \simeq 5\ \text{Hz} \tag{4.8}$$

using the parameters $\omega_j = 193.4$ THz, $n = 1.53$, $p_{13} = 0.27$, $\Omega_m = 12.46$ GHz, $\rho = 2650\ \text{kg/m}^3$, $A = \pi \cdot (70\ \mu\text{m})^2$, $L_{cr} = 4$ mm, $L_{cav} = 10$ mm. The small discrepancy could very likely stem from a non-perfect mode-overlap between the optical and acoustic mode. To obtain strong coupling in an optomechanical system, it is required for the coupling strength, G, to exceed the limit set by the optical and mechanical linewidths [35]:

$$G > \frac{\kappa + \Gamma}{2} \tag{4.9}$$

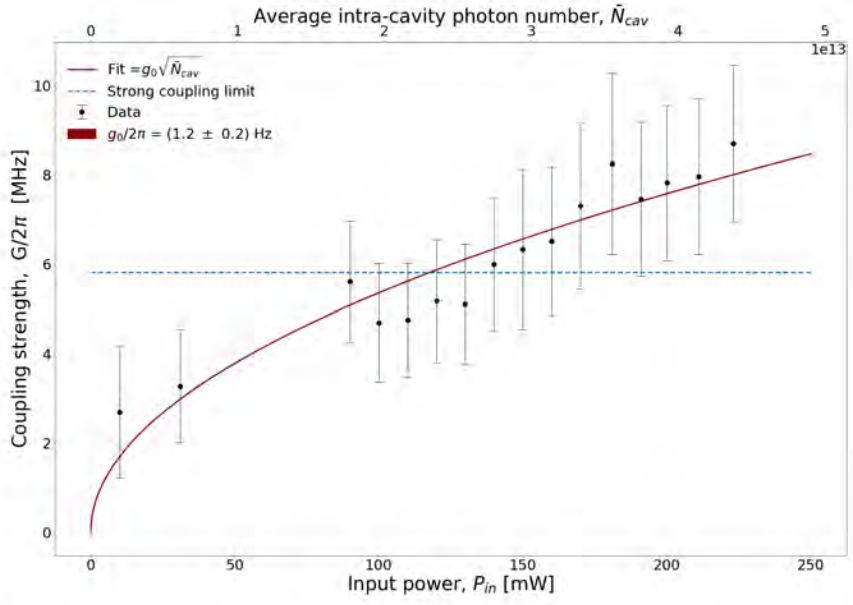

Figure 4.16: Coupling strength, G, as a function of input power, P_{in} (ordinary x-axis) and average intra-cavity photon number (secondary x-axis), $\bar{N}_{cav}$. The data is shown in black with error bars of one standard deviation. The fit is shown in red, and the blue dashed line display the strong coupling limit for this system.

For this system, the threshold for strong coupling was measured to be:

$$\frac{1}{2\pi}\frac{\kappa+\Gamma}{2} = (5.8 \pm 0.5)\ \text{MHz} \tag{4.10}$$

The threshold is represented by a blue dashed line in figure 4.16 and is exceeded for input powers around 125 mW. It is clear from the plot, that the coupling between the acoustic and optical mode is obtained well into the strong coupling regime.

4.4 Discussion and Outlook

In this chapter, it was presented how coupling between optical photons (~ 200 THz) and high frequency phonons (~ 12 GHz) from bulk acoustic waves was used to obtain both Brillouin lasing and strong photon-phonon coupling at room temperature.

For the future scope of the experiment, different macroscopic crystalline solids are planned to be tested, e.g., TeO_2 with a Brillouin frequency around 11.8 GHz and KTP, normally used for squeezing, with a Brillouin frequency around 17 GHz. Demonstrating these qualities of the system; utilizing bulk acoustic waves by optical control, one can envision new classical technologies based on this system, such as oscillators and new types of lasers. Furthermore, the system can be used to examine material parameters of a variety of transparent crystalline structures.

For equivalent optomechanical systems using high frequency bulk crystalline resonators, the one presented here, is to the authors knowledge the first to demonstrate strong coupling at room temperature. Achieving strong coupling is an important milestone working towards strong coupling measurements in the quantum regime by cooling the system to milli-Kelvin temperatures, which will be discussed in further detail in the following chapter.

Chapter 5

Cryogenic Cavity for Ground State Cooling

5.1 Introduction

In this chapter, a state-of-the-art design for operating a high frequency optomechanical system in its quantum ground state, is presented. The underlying conceptual considerations of the optomechanical cavity, consisting of the optical high finesse cavity with a plano-convex quartz crystal inside, is presented in chapter 3.

The objective of the cryogenic cavity design is, first of all, to create a robust and precisely aligned system. When cooled down, this will enable measurements in the mechanical ground state. With the mechanical eigenfrequencies of quartz around $\Omega_m \sim 12$ GHz, it is possible to reach an average phonon occupancy, $\bar{n}_{th} < 1$, when cooled to $T \sim 100$ mK, according to the Planck distribution $\bar{n}_{th} = 1/\left(\exp\left(\frac{\hbar\Omega_m}{k_B T}\right) - 1\right)$ [41], where $\hbar$ is the reduced Planck's constant and k_B is the Boltzmann constant. Thereby it is possible to reach the quantum ground state of the mechanics using standard bulk refrigeration techniques, without the use of additional laser cooling. At these temperatures the coherence length of the phonons are in the order of cm [49], and with a 4 mm long plano-convex crystal forming a phononic cavity, the phonons can achieve many coherent

round trips.

The asymmetry of the FSR spectrum, described in chapter 3, enables the selective stimulation of either the Stokes or the anti-Stokes process, thus either create or annihilate phonons. Combining this with quality factors in the order of 10^7 [30] and at a temperature low enough to be robust against thermal decoherence, enable a variety of quantum measurements. One can envision such a system developed for quantum memories, where quantum states could be read from the optical modes and stored onto the phononic modes, probing first the Stokes and subsequently the anti-Stokes process [22]. Another possibility is to perform tomography of a single phonon Fock state or transferring exotic quantum states such as cat states from the light to the acoustics [63]. An attractive application, apart from the quantum memory, is to exploit the frequency conversion to develop quantum transducers between the optical frequencies and the Gigahertz frequency range used in several of the most pursued qubit technology platforms, such as superconducting transmon qubits. [20].

5.2 Design Studies

The design of the cavity operating at milli-Kelvin temperatures is first and foremost based on the considerations described in chapter 3. To design such an optomechanical cavity for operation at milli-Kelvin temperatures, several factors need to be considered. First of all, when cooling down the cavity in the dilution fridge (Bluefors, LD), materials will contract differently depending on the coefficient of thermal expansion of the given material, which will affect the alignment. For that reason, the cavity was designed as a monolithic and cylindrical symmetric cavity, in collaboration with Kapacitet [64], who assisted to get the right dimensions and alignment for milli-Kelvin temperatures as well as the manufacturing. In figure 5.1 a Solidworks model is shown as cut-through of the cavity. The cavity consists of three main parts in brass; the central part containing the mirrors and crystal, and a part on each side of the central part containing the piezo stacks and the lenses for mode matching. Fiber-coupled GRIN lenses are mounted in both ends of the cavity. An x-y-positioning-stage is used to actively align the in-coupling beam from the GRIN lens to the cavity, where the alignment of the other GRIN lens is passive to collect the transmitted light, which by design is only used to lock the cavity and not for measuring the acoustic modes.

In chapter 4 it was described how the optical cavity mode of the room temperature cavity was detuned with respect to the mechanical mode by temperature change. As the aim is to keep the cryogenic cavity as cold as possible while measuring,

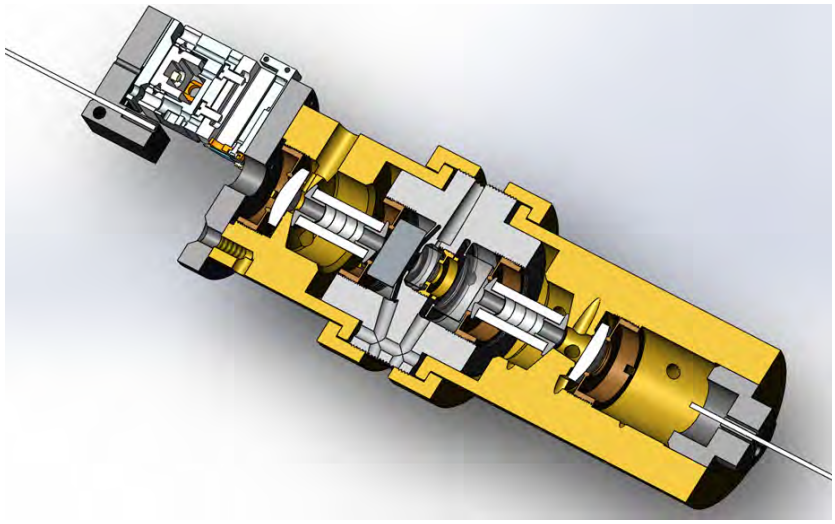

Figure 5.1: Solidworks model of the cryogenic cavity shown as a cut-through. The assembly consists of three main parts in brass; the central part containing the mirrors and crystal, and the two outer parts containing the piezo stacks and mode matching lenses. Fiber-coupled GRIN-lenses are mounted in each end of the cavity, one with active alignment using an x-y-positioning stage, the other using passive alignment.

the same approach for detuning cannot be used for the cryogenic cavity. Hence, the design criteria was to either have the possibility to move the crystal or to move the mirrors. A first suggestion for the cavity design was to place a piezo stack with an aperture inside the cavity in order to move the crystal. It turned out to not be feasible with the dimensional constraints of the cavity combined with the available piezo stack lengths and strokes. A minimum requirement for the crystal displacement at temperatures below 10 K is 500 nm − 800 nm as the displacement of the crystal will give rise to coupling to either one, two, or three acoustic modes within that range, demonstrated in [49]. With the piezo stroke decreasing to 7% of the original stroke specified at room temperature when cooled to milli-Kelvin temperatures, the choice fell on 16 mm long piezo stacks with a stroke of 11 μm at room temperature and $\sim$ 770 nm at milli-Kelvin temperatures. As an alternative solution, instead of offsetting the crystal within the cavity, the cavity was designed with two piezo stacks, one for each mirror. It gives the possibility to move both piezo stacks simultaneously and thereby keep the same cavity length, but change the crystal position, or simply move only one piezo stack and thereby change the length of the cavity.

In order to have as few degrees of freedom to align in the cryogenic environment as possible, fiber-coupled GRIN lenses are used to couple in the light. The calculations for the type and position of the standard mode matching lenses as well as the GRIN lenses included the dimensional constrains from the piezo stacks and the dilution fridge itself. Furthermore, the availability of GRIN lenses with suitable waists, was added to the dimensional constrains for the calculations. In order to find the best position and match for the standard lenses, one on each side of the cavity, as well as for both the GRIN lenses, the optical system was simulated using the ABCD matrix formalism, as described in section 3.4. The coupling efficiency, η_c, was then calculated for the E-fields of the cavity and each of the GRIN lenses [52]:

$$\eta_c = \frac{\left|\int\int E_1(x,y)\cdot E_2^*(x,y)dxdy\right|^2}{\int\int \left|E_1(x,y)\right|^2 dxdy \cdot \int\int \left|E_2(x,y)\right|^2 dxdy} \tag{5.1}$$

with the electric fields:

$$E(r,z) = E_0 \frac{w_0}{w(z)} \exp\left(\frac{-r^2}{w^2(z)}\right) \exp\left[-i\left(kz + \frac{kr^2}{2R(z)} - \arctan(z/z_R)\right)\right] \tag{5.2}$$

where E_0 is the amplitude at $z = 0, r = 0$, w_0 is the waist, $w(z)$ is the position dependent beam size, $r = \sqrt{x^2 + y^2}$ is the radial distance from the beam axis, $k = 2\pi n/\lambda$ is the wave number, $R(z)$ is the radius of curvature of the wavefront of the beam, and $z_R = \pi w_0^2 n/\lambda$ is the Rayleigh length.

The overlap between the acoustic cavity and the optical cavity with the configuration of cavity length, $L_{cav} = 10$ mm, and a crystal position relative to the in-coupling mirror at, $d_{cr} = 1$ mm, was calculated to $\eta_c = 99.3\%$. Since the measurements are done in reflection, the field overlap between the cavity and the GRIN lens for the in-coupling beam was highly prioritised. This field overlap was optimised to $\eta_c = 99.99\%$ with the best possible lens and GRIN lens position. The overlap between the transmission from the cavity and the GRIN lens used for transmission was optimised to $\eta_c = 60.6\%$. This coupling efficiency was not as prioritised as the other GRIN lens as the transmission is only used to feed back to the laser for the laser lock.

The best configuration within the design constraints is shown in figure 5.2, with the best match of lenses with focal length $f = 30$ mm to couple into the cavity and a lens with focal length $f = 40$ mm for the transmission of the cavity to focus into the GRIN lens. In figure 5.2, the GRIN lenses are displayed in light

blue, the standard lenses in dark blue, the in-coupling laser beam in green and the transmitted beam in red. The mirrors are shown in black and the crystal in the center is in red. The position $z = 0$ is set to be the position of the cavity beam waist, w_0.

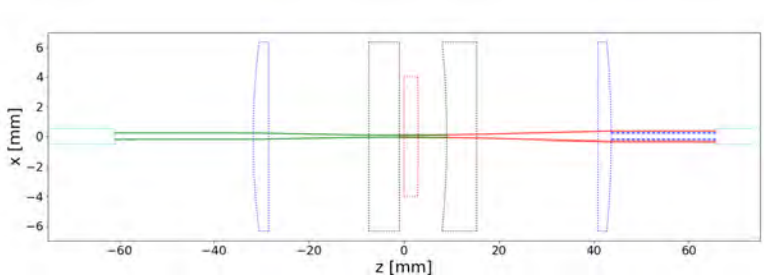

Figure 5.2: Simulation of cryogenic cavity design. GRIN lenses are in cyan, incoming beam in green, transmitted beam in red, plano-convex lenses in dashed dark blue, plano-concave mirrors in dashed black, and the plano-convex crystal in dashed red. $z = 0$ is located at the cavity beam waist, w_0.

The simulation was carried out with the measures of the first characterisations of the GRIN lenses (no. 1 and 2) with a waist, w_0, of $w_{0,1} = 211.4$ μm, and $w_{0,2} = 216.8$ μm, for the first and second GRIN lens respectively. The characterisation of the GRIN lenses are described in further detail in Appendix A. In order to obtain the best configuration in the simulation, the GRIN lens (no. 2) with the largest waist was chosen for the transmission. A zoom-in of figure 5.2 is shown in figure 5.3 to better display the field overlaps for the best configuration.

The effect on the overlap between the fields of the cavity and the GRIN lens for in-coupling was studied for different properties of the GRIN lens; the pointing error, the offset in x, y direction, the offset in z direction, and the error in waist size. The plots shown in figure 5.4 and figure 5.5 are based on the calculations presented in this chapter and in chapter 3, section 3.4, where angling and offsets of the beam are introduced.

It is shown that the overlap is > 95% within a pointing error of the GRIN lens on ±1.25 mrad in figure 5.4a and for an offset of the GRIN lens in the $x - y$ direction between ±15 μm in figure 5.4b. For a large field overlap between the cavity and the GRIN lens, a very small pointing error of the GRIN lens and a high precision in the $x - y$ plane of the in-coupling beam are thus required.

In figure 5.5a the overlap between the fields is displayed as a function of the GRIN lens offset in the z direction, where it is demonstrated that it takes a large

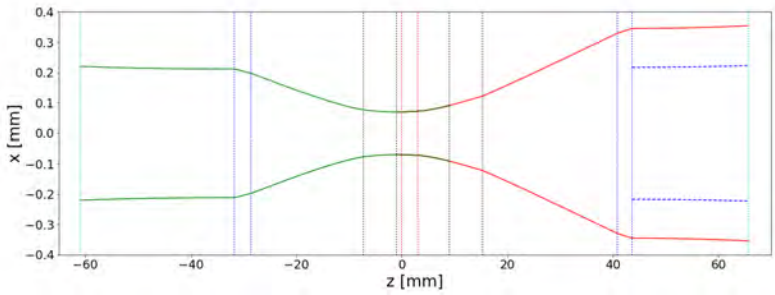

Figure 5.3: Simulation of beam propagation for the cryogenic cavity design. The GRIN lenses are in dashed light blue, lenses in dashed dark blue, mirrors in dashed black, and the crystal in dashed red. The outgoing optical beam for the first GRIN lens is in green, the propagation of the transmitted beam from the cavity to the GRIN lens is in red. The waist of the GRIN lens is in dashed blue.

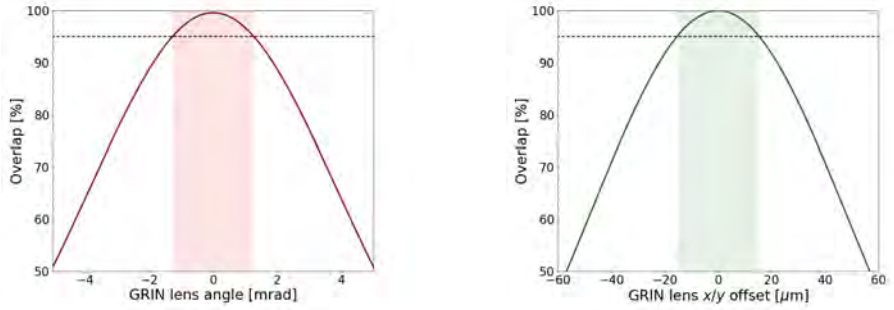

(a) **(b)**

Figure 5.4: **(a)** Overlap between the electric fields of the cavity and the GRIN lens for in-coupling as a function of the tilt of the GRIN lens (in mrad). The calculation is done with a zero $x - y$ offset of the GRIN lens. In order to get an overlap of $> 95\%$ the pointing error of the GRIN lens should be < 1.25 mrad. **(b)** Overlap between the electric fields of the cavity and the GRIN lens for in-coupling as a function of the offset in the $x - y$-plane of the GRIN lens (in μm). The calculation is done for zero tilt of the GRIN lens. In order to get an overlap of $> 95\%$ the the offset should be < 15 μm.

displacement, $\Delta z \sim 15$ mm, to decrease the overlap to $< 95\%$. Where it was shown in figure 5.4b that a displacement of the GRIN lens in the $x - y$ plane of just 20 μm would decrease the overlap to $< 95\%$, a displacement in the z direction 10 times as large, $\Delta z = 200$ μm (orange area in figure 5.5a) would cause almost no change in the overlap. The effect on the overlap from the change in waist of the GRIN lens is displayed in figure 5.5b. A change of 10% (dark blue area) or 15% (light blue area) would still result in an overlap of $\geq 99\%$.

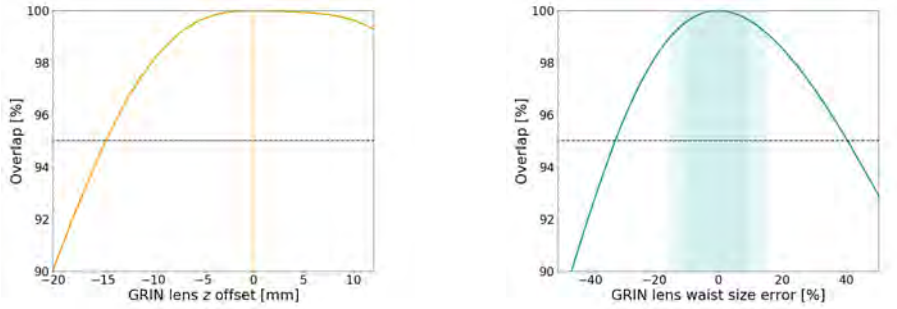

(a) **(b)**

Figure 5.5: **(a)** Overlap between electric fields of the cavity and the GRIN lens as a function of the the GRIN lens offset in z direction. A displacement of $\Delta z = 200 \mu$m (the orange area) has an unremarkable impact on the overlap. **(b)** Overlap between the electric fields of the cavity and the GRIN lens for in-coupling as a function of the GRIN lens waist error (in %). A waist error of 10% (dark blue area) and 15% (light blue area) still maintain an overlap $> 99\%$.

5.3 Design of the Cryogenic Cavity

The final cavity design was created in collaboration with Kapacitet [64], who assisted to get alignment at a very high precision and to obtain the right dimensions when cooling down the cavity, as well as the manufacturing of the cavity. The cavity is designed such that it acquires the right dimensions at milli Kelvin temperatures. To ensure the best alignment and stability, the cavity is monolithic and cylindrical symmetric. The three main parts are fabricated in brass. The central part contains the cavity mirrors (same as the room temperature cavity) and the plano-convex quartz crystal (Eksma optics), shown in figure 5.6. The mirrors and crystal are shown in grey. On each side of the mirrors, the tip

of the piezo stacks with curved retainers are shown. Very delicate cut-outs of the brass are connected to the mirrors (the grey slits that end at the edge of the curved side of the mirrors and the brown slits at the back side of each mirror). These cut-outs make the cavity flexible at small scales, such that the piezo stacks can displace the mirrors.

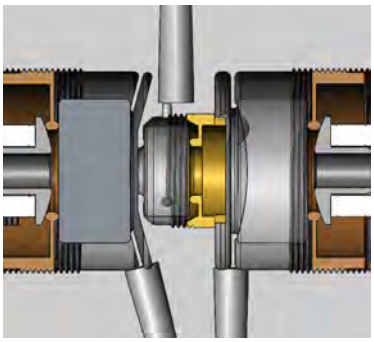

Figure 5.6: Solidworks model of the center part of the cryogenic cavity. The mirrors and plano-convex crystal are shown in grey. On each side of the mirrors the tip of the piezo stacks with curved retainers are shown.

The two brass parts on each side of the central part, contain the piezo stacks and the lenses used for mode matching. All the elements inside the three brass parts: mirrors, crystal, lenses, and piezo stacks, are aligned using the surface curvature. In figure 5.7a a Solidworks model of the piezo stack, curved retainers, mode matching lens and retainer ring is shown in "explosion view". Only the lens and retainer ring is displayed in 5.7b to show how the alignment using the surface curvature is utilized.

The piezo stacks (PI, PICMA P-080.340) selected for the cavity are multilayer ring actuators with aperture of a diameter, D_{in} = 4.5m, to allow the laser beam to pass. The dimensions of the piezos (outer diameter, D_{out} = 8m, and length L_{piezo} = 16 mm) was taken into consideration for the cavity design in general. At room temperature the stroke of the piezos are 11 μm ± 10% but decreases to ~ 7% of the original stroke when cooled to milli-Kelvin temperatures and thus permit a stroke ~ 770 nm.

In figure 5.8 the entire assembly of the cavity is shown with the central part, described above, as well as the two outer brass parts, containing the piezo stacks and mode matching lenses. The cavity is assembled from the center outwards, see Appendix B. For the alignment of the in-coupling beam, an x-y cryo-positioning stage (JPE, CBS5) is used. The positioning-stage (shown in light blue) made of stainless steel, has a range of 5.5 mm and a minimum step

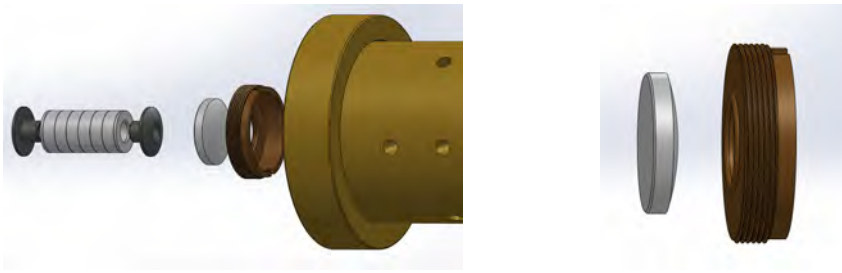

(a) (b)

Figure 5.7: **(a)** Solidworks model of piezo stack, curved retainers, lens, and retainer ring in "explosion view". **(b)** Solidworks model of the lens and retainer ring, showing the alignment using the surface curvature.

size of 50 nm at 4 Kelvin. The x-y-stage provides active alignment of the GRIN lens placed inside a custom made GRIN less holder made of stainless steel. The GRIN lens holder assures the alignment and precision of the GRIN lens as well as protecting the fragile component. A similar GRIN lens holder is designed for passive alignment of the transmission, shown to the very right in figure 5.8. Holes for venting are symmetrically distributed on every part of the cavity design to mitigate out-gassing in the dilution fridge. One of the cut-outs will accommodate the temperature sensor (Lakeshore, RX-102A-AA).

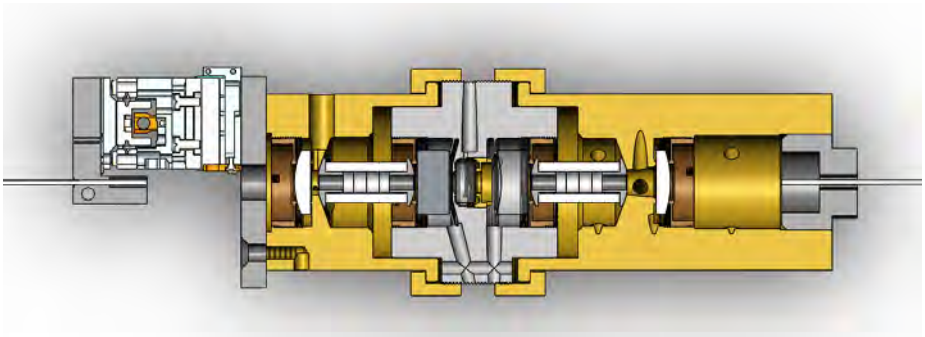

Figure 5.8: Solidworks model of the cryogenic cavity, displaying the three main parts made in brass; the central part containing the mirrors and crystal (in grey) and the outer parts containing the piezo stacks and mode matching lenses (white). In both ends of the cavity, fiber-coupled GRIN lenses are mountet. One of the GRIN lenses are actively aligned with and x-y positioning stage (light blue).

5.4 Experimental Setup

The experimental setup is to a high extent similar to the one presented in chapter 4. The measurement scheme and equipment are the same, but the laser beam is instead sent to the cavity inside the dilution fridge.

The very first tests were made to couple in light to the cavity at room temperature. Early experiments revealed the need for extra degrees of freedom for the in-coupling GRIN lens (see Appendix A), which was provided by adding a tip-tilt stage to the system. The mirror mount will be pre-aligned at room temperature, and has no active alignment at low temperature. The mirror mount was added to the cavity design with adapters in order to be mounted properly. In figure 5.9a a Solidworks model is shown of the added mirror mount and adapters mounted in between the x-y-stage and the GRIN lens holder, where the actual components are depicted in figure 5.9b. In figure 5.10 the entire assembly with the added mirror mount is shown inside the dilution fridge.

(a) **(b)**

Figure 5.9: In order to get more degrees of freedom (tip-tilt) of the in-coupling light, a modification of the cavity design was performed, constituting a mirror mount and adapters in between x-y-stage and the GRIN lens holder. The modification is shown as a Solidworks model in **(a)** of the mirror mount (grey) added to the design in between the x-y-stage (light blue) and the GRIN lens holder (dark grey) with adapters (blue) in order to be mounted. The actual components are depicted in **(b)** with the mirror mount added to the design in between the x-y-stage and the GRIN lens holder.

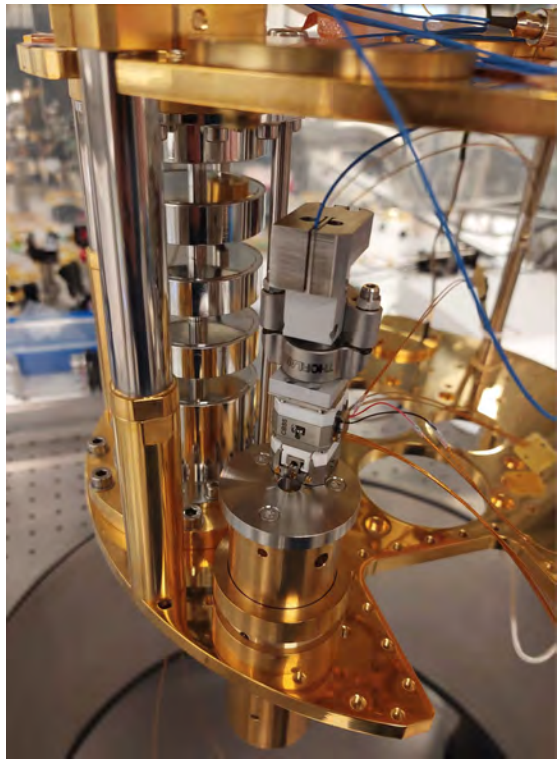

Figure 5.10

Figure 5.11: The entire cavity assembly with the added mirror mount inside the dilution fridge.

5.4.1 Characterisation of the Cryogenic Cavity at Room Temperature

The initial successful attempt to achieve modes in the cryogenic cavity, was done by coupling into the bare optical cavity without the crystal inside, using free space optics at room temperature, shown in figure 5.12. Here, the cavity assembly consists of the central brass parts, containing only the two mirrors and no crystal, mounted onto one of the outer brass part, containing only the mode matching lens for in-coupling (not the piezo stack).

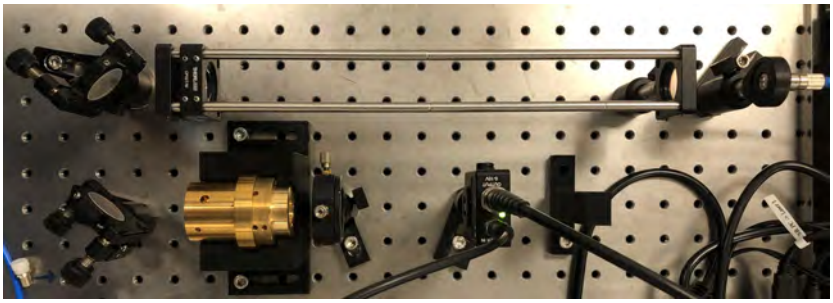

Figure 5.12: Experimental setup for the cryogenic cavity coupling into the bare optical cavity without the crystal, using free space optics. The cavity assembly consists of the central brass part, containing only the mirrors (not the crystal) and one outer brass part containing only the in-coupling mode matching lens (not the piezo stack). Light is sent from a collimation package through a beam expander to achieve the mode size expected from a GRIN lens.

To measure the FSR, a wavelength scan was performed between 1550.25 nm - 1550.65 nm, shown in figure 5.13. Four fundamental modes and a few misalignment modes are shown. The distance between the fundamental cavity modes are $\sim$ 0.111 nm corresponding to an FSR of $\sim$ 13.85 GHz. As the wavelength scan is not completely linear, the length of the cavity from these four modes was found to L_{cav} = (10.82 ± 0.06) mm from this characterisation. The cavity length extracted from the CAD drawings is 10.39 mm. From these first characterisations in room temperature, there is a discrepancy of $\sim$ 400 μm, which can easily be acquired when assembling the mirrors inside the cavity, see Appendix B. Furthermore, the piezo stacks were not inside the cavity assembly while acquiring the data, and the pressure from the piezo stacks on each mirror might compress the cavity slightly, leading to a slightly shorter cavity length. The cavity is designed to contract into the right dimensions and alignment at milli-Kelvin temperatures, where the measures are expected to be even more precise. When the crystal is introduced to the cavity, the path of the light will

increase, resulting in a slightly smaller FSR and the asymmetry of the FSR will add a spread of ~ ±2 GHz, and is thus expected to cover the Brillouin frequency within the FSR-range.

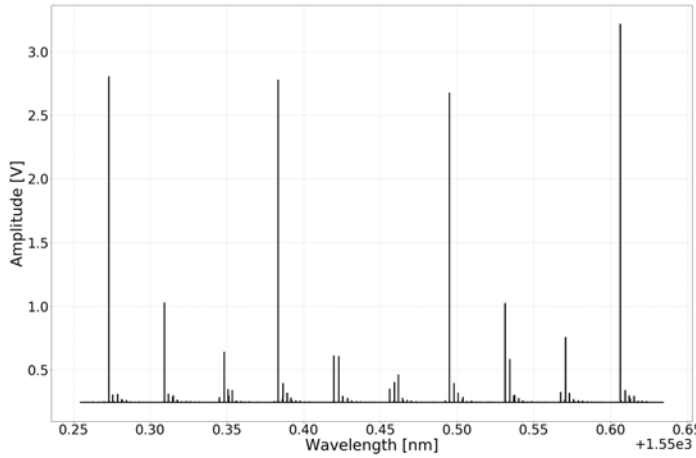

Figure 5.13: Initial characterisation of the cryogenic cavity using a wavelength scan between 1550.25 nm - 1550.65 nm. Four fundamental modes are displayed, while a few misalignment peaks appears as well. The distance between the fundamental cavity modes are ~ 0.111 nm.

The linewidth of the cryogenic cavity was measured using sidebands generated by an EOM at 10 MHz and was characterized to $\kappa = (1.21 \pm 0.02)$ MHz, shown in figure 5.14. Using the specifications of the mirrors, the linewidth was calculated to $\kappa = \text{FSR}/\mathcal{F} = 1.19$ MHz at a cavity length of $L_{cav} = 10.82$ MHz, where $\text{FSR} = c/2L_{cav}$ and $\mathcal{F} = 2\pi/(T_1 + T_2)$, with $T_{1,2}$ being the transmission of the two mirrors respectively.

The next step of the experiment is, first of all, to obtain a signal with the entire cavity assembly at room temperature and then obtain a signal when cooling the cryogenic cavity in the dilution fridge.

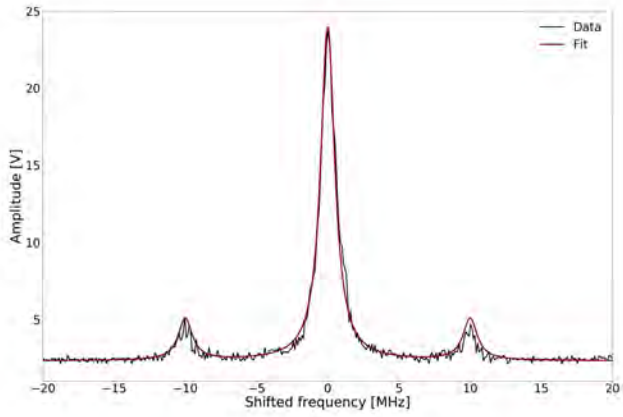

Figure 5.14: Characterizing the linewidth of the bare optical cavity (no crystal inside the cavity), using sidebands of 10 MHz, the linewidth was measured to $\kappa = (1.21 \pm 0.02)$ MHz.

Chapter 6

Conclusion and Prospects

In this thesis, the development of two optomechanical cavities was presented; one for operation at room temperatures, the other for operation at milli-Kelvin temperatures. Both cavities were designed with crystalline quartz inside a high-finesse optical cavity, the first with a flat-flat-faceted crystal, the latter with a plano-convex shaped crystal. The simulations behind the physical design criteria were presented as well as the actual designs, demonstrating the advantage of the asymmetric mode spacing of the optomechanical cavities.

For the cavity operating at room temperature, Brillouin lasing was demonstrated with a lasing threshold at input powers of ~ 15 mW. Furthermore, strong coupling between the optics and bulk acoustic waves in the crystal was demonstrated with a mode splitting $2G > (\kappa + \Gamma)$, where the optical linewidth was measured to $\kappa/2\pi = (1.00 \pm 0.03)$ MHz and an acoustic linewidth, $\Gamma/2\pi = (10.6 \pm 0.9)$ MHz. The mode splitting was demonstrated for several different input powers, allowing to estimate the different coupling rates and a single photon coupling rate of $g_0/2\pi \simeq (1.2 \pm 0.2)$ Hz. Strong coupling between optics and acoustics at room temperature was demonstrated here for the first time for this type of optomechanical cavity. This robust system, both allowing for Brillouin lasing and strong coupling at room temperatures, makes examination of different crystalline materials an exciting, viable possibility. Materials planned to be tested in the system are the high frequency crystalline materials; TeO_2 with a Brillouin frequency around 11.8 GHz and KTP, normally used for squeezing

and with a Brillouin frequency around 17 GHz. Tests of both new materials are presumably straight forward to perform in the existing setup by adjusting the length of the optical cavity by adding or removing spacers.

In the last part of the thesis, a state-of-the-art cryogenic cavity design for ground state cooling was presented, as well as the first characterisations of the cavity. For the continuation of the project, the first objective for this system will be to achieve quantum ground state operation, which would be novel for an optomechanical cavity using bulk acoustic waves. Inside the optical cavity, the plano-convex shaped quartz crystal allows for multiple round trips for the phonons, when cooled to milli-Kelvin temperatures. Obtaining coherent long-lived phonon modes at ground state operation will both enable probing of fundamental physics and permit developments of several cutting edge applications.

Indeed, a lot of exciting measurements await after succeeding ground state operation of the system; perform optomechanically induced transparency and absorption, achieve phonon lasing with a very narrow linewidth of the acoustics ($\Gamma \ll \kappa$), and observe of strong coupling between the acoustics and optics at the ground state. Furthermore, one could envision coherent state transfer of non-classical states such as squeezed states or cat states from the optics onto the acoustics, or perform tomography of a single phonon Fock state, which would enable exploration of quantum behaviour within macroscopic objects [65].

Finally, this system enables advancement of a variety of hybrid quantum technologies. In the quantum coherent strong coupling regime, deterministic state swaps between the photons and phonons could be utilised for quantum information storage, i.e. quantum memories. Furthermore, bulk acoustic waves have been demonstrated to couple strongly to superconducting qubits [66], [67], and therefore presents a strong candidate for quantum transducers.

Appendix A

GRIN lens Characterizations

Gradient index (GRIN) lenses are lenses, where the index of refraction decreases in radial direction from the axis, making it possible for the lens to have a flat surface and in this case, to be mounted on a fiber. The GRIN-lenses (from Grintech) used for the this work, were customised to get the best possible pointing stability, preferably between 1-2 mrad and a waist on 250 microns. It was experienced, that the GRIN lenses were very fragile and unfortunately only a few of the ordered lenses were within the pointing error (measured beam angle in respect to the fiber ferrule), characterized by Grintech and verified subsequently for this work.

The waist, ω_0, and the position of the waist, z_0, were characterized using the knife-edge technique [68] (using a Thorlabs beam profiler), with the simple setup shown in figure A.2. The position, $z = 0$, was determined to be at the end of the GRIN lens. In figure A.1 one characterization is shown, where the beam size, ω_z, is measured at different positions, z, in order to determine the waist, ω_0, and the position of the waist, z_0, of the GRIN lens. The data points are fitted to [52]:

$$\omega(z) = \omega_0 \sqrt{1 + \left(\frac{z - z_0}{z_R}\right)^2} \tag{A.1}$$

where $z_R = \pi\omega_0^2/\lambda$ is the Rayleigh length, and λ, the wavelength of the laser beam. In table A.1, the characterizations of the different GRIN lenses are shown.

GRIN lens no.	ω_0 [μm]	z_0 [mm]	Pointing error [mrad]
1	211.4	26	4
2	216.8	22	8
3	178.7	-68	4.6
4	180.1	-66	1.0
5	178.4	-68	2.1
6	201.9	-56	1
7	210.2	-55	2
8	202.8	-62	2

Table A.1: Measured waist, ω_0, position of the waist, z_0, and pointing error for the different GRIN lenses.

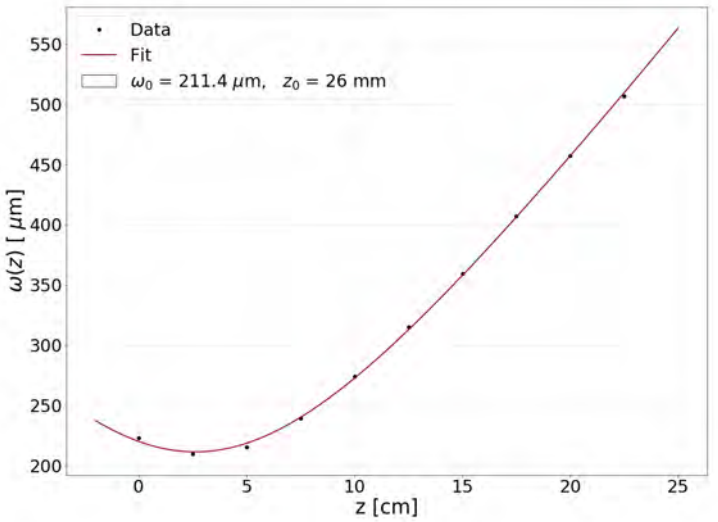

Figure A.1: Knife-edge measurement of a GRIN lens (no. 1). The beam size $\omega(z)$ is measured as a function of the position z (data in black dots) in order to determine the waist ω_0 and position of the waist z_0 by fitting the data (in red).

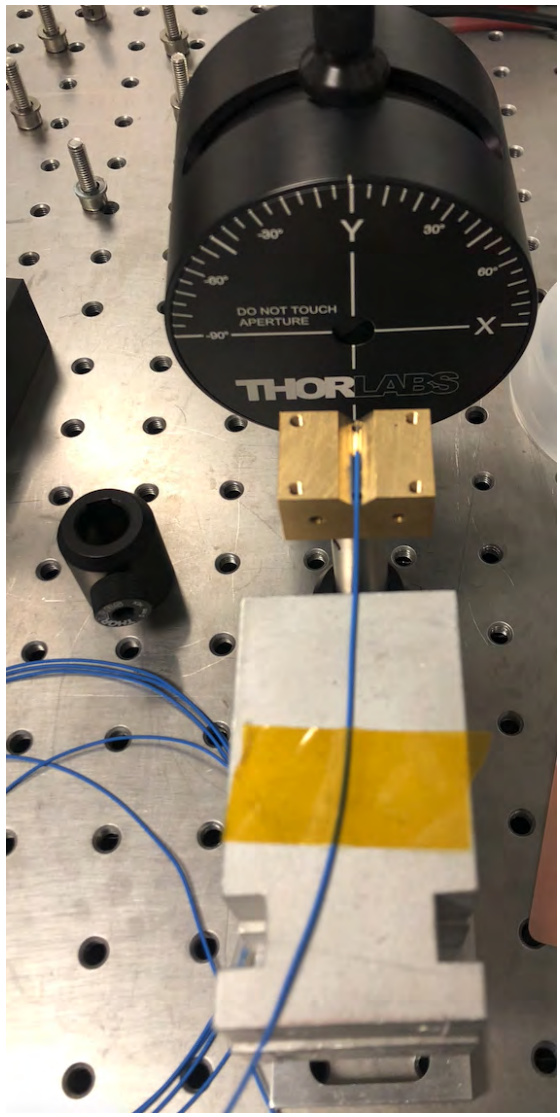

Figure A.2: Setup for characterization of the GRIN lenses. The GRIN lens at the end of the fiber, falls into the v-groove of the brass holder in order to align it. The measurements were done with a beam profiler from Thorlabs.

Appendix B

Assembly of the Cryogenic Cavity

The monolithic cryogenic cavity is assembled part by part from the center. In figure B.1 the center part of the cavity, containing the mirrors and crystal, is shown with the assembly tool (black). The assembly tool is a 3D printed tool, used for guiding and (lightly) tightening the mirrors and crystal into the right position. In order to get a proper alignment of the mirrors and crystal, the cavity is gently tapped on the side, such that the curvature aligns with the retaining rings, fabricated for this purpose.

Figure B.1: Center part of the cryogenic cavity, containing the two mirrors and the crystal, shown with the assembling tool (black).

Bibliography

[1] R. P. Feynman, "Simulating physics with computers," *International Journal of Theoretical Physics*, vol. 21, no. 6-7, pp. 467–488, 1982.

[2] A. J. Leggett, "Testing the limits of quantum mechanics: Motivation, state of play, prospects," *Journal of Physics Condensed Matter*, vol. 14, no. 15, 2002.

[3] I. Pikovski, M. R. Vanner, M. Aspelmeyer, M. S. Kim, and C. Brukner, "Probing planck-scale physics with quantum optics," *Nature Physics*, vol. 8, no. 5, pp. 393–397, 2012.

[4] T. Westphal, H. Hepach, J. Pfaff, and M. Aspelmeyer, "Measurement of gravitational coupling between millimeter-sized masses," *Nature*, vol. 591, 2020.

[5] J. Kepler, "De cometis libelli tres," *Typis Andreae Apergiri*, 1619.

[6] A. Einstein and J. Laub, "On the ponderomotive forces exerted on bodies at rest in electromagnetic field," *Annalen der Physik*, vol. 26, p. 541, 1908.

[7] R. Frisch, "Experimenteller Nachweis des Einsteinschen Strahlungsrückstoßes," *Zeitschrift für Physik*, vol. 86, no. 1-2, pp. 42–48, 1933.

[8] R. A. Beth, "Mechanical detection and measurement of the angular momentum of light," *Optical Angular Momentum*, pp. 10–20, 2016.

[9] L. Brillouin, "Diffusion de la lumière et des rayons x par un corps transparent homogène," *Annales de physique*, vol. 9, no. 17, pp. 88–122, 1922.

[10] L. Mandelstam, "Light scattering by inhomogeneous media," *Zh. Russ. Fiz-Khim. Ova*, vol. 58, no. 381, p. 146, 1926.

[11] E. Gross, "Change of wave-length of light due to elastic heat waves at scattering in liquids," *Nature*, vol. 126, no. 3171, pp. 201–202, 1930.

[12] C. F. Ockeloen-Korppi, E. Damskägg, J. M. Pirkkalainen, M. Asjad, A. A. Clerk, F. Massel, M. J. Woolley, and M. A. Sillanpää, "Stabilized entanglement of massive mechanical oscillators," *Nature*, vol. 556, no. 7702, pp. 478–482, 2018.

[13] R. Riedinger, A. Wallucks, I. Marinković, C. Löschnauer, M. Aspelmeyer, S. Hong, and S. Gröblacher, "Remote quantum entanglement between two micromechanical oscillators," *Nature*, vol. 556, no. 7702, pp. 473–477, 2018.

[14] S. Kotler, G. A. Peterson, E. Shojaee, F. Lecocq, K. Cicak, A. Kwiatkowski, S. Geller, S. Glancy, E. Knill, R. W. Simmonds, J. Aumentado, and J. D. Teufel, "Direct observation of deterministic macroscopic entanglement," *Science*, vol. 372, no. 6542, pp. 622–625, 2021.

[15] R. A. Thomas, M. Parniak, C. Østfeldt, C. B. Møller, C. Bærentsen, Y. Tsaturyan, A. Schliesser, J. Appel, E. Zeuthen, and E. S. Polzik, "Entanglement between distant macroscopic mechanical and spin systems," *Nature Physics*, 2020.

[16] N. Fiaschi, B. Hensen, A. Wallucks, R. Benevides, J. Li, T. P. Alegre, and S. Gröblacher, "Optomechanical quantum teleportation," *Nature Photonics*, vol. 15, no. 11, pp. 817–821, 2021.

[17] B. P. Abbott, R. Abbott, T. Abbott, M. Abernathy, F. Acernese, K. Ackley, C. Adams, T. Adams, P. Addesso, R. Adhikari, *et al.*, "Observation of gravitational waves from a binary black hole merger," *Physical review letters*, vol. 116, no. 6, p. 061102, 2016.

[18] A. Einstein, "Näherungsweise Integration der Feldgleichungen der Gravitation," *Sitzungsberichte der Königlich Preußischen Akademie der Wissenschaften (Berlin)*, vol. 1, pp. 688–696, 1916.

[19] A. Einstein, "Über gravitationswellen," *Sitzungsberichte der Königlich Preußischen Akademie der Wissenschaften (Berlin)*, vol. 1, p. 154, 1918.

[20] Y. Chu and S. Gröblacher, "A perspective on hybrid quantum opto- and electromechanical systems," *Applied Physics Letters*, vol. 117, no. 15, 2020.

[21] B. Stiller, M. Merklein, C. Wolff, K. Vu, P. Ma, S. J. Madden, and B. J. Eggleton, "Coherently refreshing hypersonic phonons for light storage," *Optica*, vol. 7, no. 5, p. 492, 2020.

[22] A. Wallucks, I. Marinković, B. Hensen, R. Stockill, and S. Gröblacher, "A quantum memory at telecom wavelengths," *Nature Physics*, vol. 16, no. July, 2020.

[23] A. Rueda, F. Sedlmeir, M. C. Collodo, U. Vogl, B. Stiller, G. Schunk, D. V. Strekalov, C. Marquardt, J. M. Fink, O. Painter, G. Leuchs, and H. G. L. Schwefel, "Efficient microwave to optical photon conversion: an electro-optical realization," *Optica*, vol. 3, no. 6, p. 597, 2016.

[24] A. P. Higginbotham, P. S. Burns, M. D. Urmey, R. W. Peterson, N. S. Kampel, B. M. Brubaker, G. Smith, K. W. Lehnert, and C. A. Regal, "Harnessing electro-optic correlations in an efficient mechanical converter," *Nature Physics*, vol. 14, no. 10, pp. 1038–1042, 2018.

[25] F. Arute, K. Arya, R. Babbush, D. Bacon, J. C. Bardin, R. Barends, R. Biswas, S. Boixo, F. G. Brandao, D. A. Buell, *et al.*, "Quantum supremacy using a programmable superconducting processor," *Nature*, vol. 574, no. 7779, pp. 505–510, 2019.

[26] H. J. Kimble, "The quantum internet," *Nature*, vol. 453, no. 7198, pp. 1023–1030, 2008.

[27] M. Rossi, D. Mason, J. Chen, Y. Tsaturyan, and A. Schliesser, "Measurement-based quantum control of mechanical motion," *Nature*, vol. 563, no. 7729, pp. 53–58, 2018.

[28] S. Barzanjeh, E. S. Redchenko, M. Peruzzo, M. Wulf, D. P. Lewis, G. Arnold, and J. M. Fink, "Stationary entangled radiation from micromechanical motion," *Nature*, vol. 570, no. 7762, pp. 480–483, 2019.

[29] U. Delić, M. Reisenbauer, K. Dare, D. Grass, V. Vuletić, N. Kiesel, and M. Aspelmeyer, "Cooling of a levitated nanoparticle to the motional quantum ground state," *Science*, vol. 367, no. 6480, pp. 892–895, 2020.

[30] W. H. Renninger, P. Kharel, R. O. Behunin, and P. T. Rakich, "Bulk crystalline optomechanics," *Nature Physics*, vol. 14, pp. 601–607, 6 2018.

[31] P. Kharel, G. I. Harris, E. A. Kittlaus, W. H. Renninger, N. T. Otterstrom, J. G. Harris, and P. T. Rakich, "High-frequency cavity optomechanics using bulk acoustic phonons," *Science Advances*, vol. 5, no. 4, pp. 1–9, 2019.

[32] P. Kharel, Y. Chu, D. Mason, E. A. Kittlaus, N. T. Otterstrom, S. Gertler, and P. T. Rakich, "Multimode Strong Coupling in Cavity Optomechanics," *Physical Review Applied*, vol. 18, no. 2, p. 1, 2022.

[33] U. L. Andersen, T. Gehring, C. Marquardt, and G. Leuchs, "30 Years of Squeezed Light Generation," *Physica Scripta*, vol. 91, no. 5, 2016.

[34] R. Y. Teh, S. Kiesewetter, P. D. Drummond, and M. D. Reid, "Creation, storage, and retrieval of an optomechanical cat state," *Physical Review A*, vol. 98, no. 6, pp. 1–18, 2018.

[35] G. Enzian, M. Szczykulska, J. Silver, L. Del Bino, S. Zhang, I. A. Walmsley, P. Del'Haye, and M. R. Vanner, "Observation of Brillouin optomechanical strong coupling with an 11 GHz mechanical mode," *Optica*, vol. 6, no. 1, p. 7, 2019.

[36] D. Høj, F. Wang, W. Gao, U. B. Hoff, O. Sigmund, and U. L. Andersen, "Ultra-coherent nanomechanical resonators based on inverse design," *Nature Communications*, vol. 12, no. 1, pp. 1–8, 2021.

[37] E. Verhagen, S. Deléglise, S. Weis, A. Schliesser, and T. J. Kippenberg, "Quantum-coherent coupling of a mechanical oscillator to an optical cavity mode," *Nature*, vol. 482, no. 7383, pp. 63–67, 2012.

[38] X. He, G. I. Harris, C. G. Baker, A. Sawadsky, Y. L. Sfendla, Y. P. Sachkou, S. Forstner, and W. P. Bowen, "Strong optical coupling through superfluid Brillouin lasing," *Nature Physics*, vol. 16, no. 4, pp. 417–421, 2020.

[39] M. Aspelmeyer, T. J. Kippenberg, and F. Marquardt, "Cavity optomechanics," *Reviews of Modern Physics*, vol. 86, no. 4, pp. 1391–1452, 2014.

[40] Schmoele, "Cavity optomechanics." https://commons.wikimedia.org/wiki/File:Cavity_Optomechanics.png. Accessed: 2022-11-30.

[41] C. Kittel and P. McEuen, "Introduction to Solid State Physics," *John Wiley & Sons*, 2018.

[42] C. W. Wolff, M. J. A. Smith, B. Stiller, and C. G. Poulton, "Invited tutorial: Brillouin scattering – theory and experiment," *Journal of the Optical Society of America B*, vol. 38, no. 4, pp. 1–26, 2021.

[43] R. W. Boyd, "Nonlinear Optics," *Academic press*, 2014.

[44] A. Yariv, "Quantum theory for parametric interactions of light and hypersound," *IEEE Journal of Quantum Electronics*, vol. 1, no. 1, pp. 28–36, 1965.

[45] R. Chiao, C. Townes, and B. Stoicheff, "Stimulated brillouin scattering and coherent generation of intense hypersonic waves," *Physical Review Letters*, vol. 12, no. 21, p. 592, 1964.

[46] I. S. Grudinin, A. B. Matsko, and L. Maleki, "Brillouin lasing with a CaF2 whispering gallery mode resonator," *Physical Review Letters*, vol. 102, no. 4, pp. 1–4, 2009.

[47] W. H. Renninger, P. Kharel, R. O. Behunin, and P. T. Rakich, "Bulk crystalline optomechanics - supplementary," *Nature Physics*, vol. 14, no. 6, pp. 601–607, 2018.

[48] W. P. Bowen and G. J. Milburn, "Quantum Optomechanics," *CRC press*, 2015.

[49] P. Kharel, G. I. Harris, E. A. Kittlaus, W. H. Renninger, N. T. Otterstrom, J. G. Harris, and P. T. Rakich, "Supplementary: High-frequency cavity optomechanics using bulk acoustic phonons," *Science Advances*, vol. 5, no. 4, 2019.

[50] H. Bachor and T. C. Ralph, "A Guide to Experiments in Quantum Optics," *John Wiley & Sons*, 2019.

[51] S. Gröblacher, K. Hammerer, M. R. Vanner, and M. Aspelmeyer, "Observation of strong coupling between a micromechanical resonator and an optical cavity field," *Nature*, vol. 460, no. 7256, pp. 724–727, 2009.

[52] A. Yariv and P. Yeh, *Photonics: Optical Electronics in Modern Communications*. Oxford university press, 2007.

[53] W. Sellmeier, "Zur erkarung der abnormen farbenfolge im spectrum einiger substanzen," *Annalen der Physik und Chemie*, vol. 219, pp. 272–282, 1871.

[54] J. M. Binder, A. Stark, N. Tomek, J. Scheuer, F. Frank, K. D. Jahnke, C. Müller, S. Schmitt, M. H. Metsch, T. Unden, T. Gehring, A. Huck, U. L. Andersen, L. J. Rogers, and F. Jelezko, "Qudi: A modular python suite for experiment control and data processing," *SoftwareX*, vol. 6, pp. 85–90, 2017.

[55] R. J. Barlow, "Statistics, A Guide to the Use of Statistical Methods in the Physical Sciences," *John Wiley & Sons*, 1999.

[56] N. T. Otterstrom, R. O. Behunin, E. A. Kittlaus, Z. Wang, and P. T. Rakich, "A silicon Brillouin laser," *Science*, vol. 360, no. 6393, pp. 1113–1116, 2018.

[57] A. Schliesser, "Cavity Optomechanics and Optical Frequency Comb Generation with Silica Whispering-Gallery-Mode Microresonators," *PhD Thesis*, 2009.

[58] G. Bahl, J. Zehnpfennig, M. Tomes, and T. Carmon, "Stimulated optomechanical excitation of surface acoustic waves in a microdevice," *Nature Communications*, vol. 2, no. 1, 2011.

[59] I. S. Grudinin, H. Lee, O. Painter, and K. J. Vahala, "Phonon laser action in a tunable two-level system," *Physical Review Letters*, vol. 104, no. 8, pp. 2–5, 2010.

[60] G. P. A. Enzian, "Brillouin cavity optomechanics with whispering-gallery microresonators," *PhD Thesis*, 2020.

[61] K. Riley and M. Hobson, "Essential mathematical methods for the physical sciences," *Cambridge University Press*, 2011.

[62] J. R. Taylor, "Introduction to error analysis, the study of uncertainties in physical measurements," *University Science Books*, 1997.

[63] I. Shomroni, L. Qiu, and T. J. Kippenberg, "Optomechanical generation of a mechanical catlike state by phonon subtraction," *Physical Review A*, vol. 101, no. 3, 2020.

[64] "Kapacitet." https://kapacitet.dk. Accessed: 2022-11-25.

[65] M. R. Vanner, I. Pikovski, and M. S. Kim, "Towards optomechanical quantum state reconstruction of mechanical motion," *Annalen der Physik*, vol. 527, no. 1-2, pp. 15–26, 2015.

[66] Y. Chu, P. Kharel, W. H. Renninger, L. D. Burkhart, L. Frunzio, P. T. Rakich, and R. J. Schoelkopf, "Quantum acoustics with superconducting qubits," *Science*, vol. 358, no. 6360, pp. 199–202, 2017.

[67] Y. Chu, P. Kharel, T. Yoon, L. Frunzio, P. T. Rakich, and R. J. Schoelkopf, "Creation and control of multi-phonon Fock states in a bulk acoustic-wave resonator," *Nature*, vol. 563, no. 7733, pp. 666–670, 2018.

[68] Y. Suzaki and A. Tachibana, "Measurement of the μm sized radius of Gaussian laser beam using the scanning knife-edge," *Applied optics*, vol. 14, no. 12, pp. 2809–2810, 1975.